

#### **BRNO UNIVERSITY OF TECHNOLOGY**

VYSOKÉ UČENÍ TECHNICKÉ V BRNĚ

#### CENTRAL EUROPEAN INSTITUTE OF TECHNOLOGY BUT

STŘEDOEVROPSKÝ TECHNOLOGICKÝ INSTITUT VUT

# MOLECULAR SELF-ASSEMBLY ON SURFACES: THE ROLE OF COVERAGE, SURFACE ORIENTATION AND KINETICS

MOLEKULÁRNÍ SAMOUSPOŘÁDÁVÁNÍ NA POVRŠÍCH: ROLE POKRYTÍ, ORIENTACE POVRCHU A KINETIKY

#### **DOCTORAL THESIS**

DIZERTAČNÍ PRÁCE

AUTHOR

**Anton Olegovich Makoveev** 

**AUTOR PRÁCE** 

SUPERVISOR

doc. Ing. Jan Čechal, Ph.D.

ŠKOLITEL

**BRNO 2023** 

#### Abstract

Molecular self-assembly is a sophisticated natural phenomenon based on the principles of supramolecular chemistry. Not surprisingly, it has been harnessed for constructing molecular systems on surfaces. Although the field of on-surface molecular self-assembly is quite mature, it still lacks comprehensive systematic knowledge comprising universal parametric models. In this regard, we present the work aiming to shed some light on the parameter dependence of molecular self-assembly on surfaces. The first parameter we discuss is aimed at the influence of diffusion-limited conditions. For that, 4,4'-biphenyldicarboxylic acid (BDA) self-assembly on Ag(001) at complete-monolayer coverage has been investigated and compared to the self-assembly at sub-monolayer coverage. We further discuss the role of surface orientation. To do so, a comparative study of BDA self-assembly on Ag(001)and Ag(001) is put on the table. Finally, we address the kinetics of on-surface process and how it can be flexibly adjusted by non-thermal activation means. For this purpose, research on the kinetics of BDA deprotonation reaction induced by a low-energy electron beam is demonstrated. We believe that our work brings an additional piece of knowledge into the systematic picture of molecular self-assembly on surfaces and makes a step toward the development of the holistic parametric models.

#### Abstrakt

Molekulární samouspořádávání je sofistikovaný přírodní jev založený na principech supramolekulární chemie. Není divu, že byl využit ke konstrukci molekulárních systémů na površích. Ačkoli je oblast molekulární samouspořádávání na površích poměrně vyspělá, stále ještě chybí ucelené systematické poznatky zahrnující např. univerzální parametrické modely. V této souvislosti předkládáme práci, jejímž cílem je objasnit závislost molekulárního samouspořádávání na površích na vnějších parametrech. Nejprve se zabýváme vlivem difuzně omezených podmínek. Za tímto účelem bylo zkoumáno samouspořádávání kyseliny 4,4'-bifenyldikarboxylové (BDA) na Ag(001) při úplném pokrytí monovrstvou a porovnáno se samouspořádávání při submonovrstevném pokrytí. Dále diskutujeme roli orientace povrchu. Za tímto účelem je předložena srovnávací studie samouspořádávání BDA na Ag(001) a Ag(001). Nakonec se zabýváme kinetikou procesu na povrchu a tím, jak ji lze ovlivnit netermální aktivací. Toto je demonstrováno na studiu kinetiky deprotonační reakce BDA vyvolané nízkoenergetickým elektronovým svazkem. Věříme, že naše práce přináší nové poznatky do systematického obrazu samouspořádávání molekul na površích a je tak významným krokem k vývoji ucelených parametrických modelů.

#### Keywords

Molecular self-assembly, BDA, diffusion-limited conditions, Ag(100), Ag(111), kinetics

#### Klíčová slova

Molekulární samouspořádávání, BDA, difuzně omezené podmínky, Ag(100), Ag(111), kinetika

MAKOVEEV, A. O. Molecular self-assembly on surfaces: the role of coverage, surface orientation and kinetics. Brno University of Technology, Central European Institute of Technology BUT, 2023. 169 p. Thesis supervisor: doc. Ing. Jan Čechal, Ph.D.

### Contents

In	trodi	uction	1
1.		ecular self-assembly Thermodynamics and kinetics of molecular self-assembly on surfaces	<b>3</b>
		1.1.1. Thermodynamic aspects of nucleation and growth in self-assembled molecular systems on surfaces	7
		1.1.2. Kinetic aspects of nucleation and growth in self-assembled molecular systems on surfaces	8
	1.2.	The electron beam as a non-thermal activation tool of on-surface reactions 1.2.1. Electron-molecule interaction	13 13
2.	Exp	perimental methods	18
	2.1.	UHV cluster and sample preparation	18
	2.2.	Scanning tunneling microscopy	18
	2.3.	X-ray photoelectron spectroscopy	19
	2.4.	Low-energy electron microscopy/diffraction	19
3.	Mol	ecular self-assembly at high coverage	20
	3.1.	Self-assembly of BDA on $Ag(001)$ at submonolayer coverage	20
	3.2.	Phase transformations in a complete monolayer of BDA on $Ag(001)$	21
4.		e of substrate orientation  Role of phase stabilization and surface orientation in BDA self-assembly	25
	4.1.	and transformation on silver substrates	25
<b>5</b> .	Non	n-thermal activation of surface processes	28
	5.1.	Kinetic control of self-assembly using a low-energy electron beam	28
Co	onclu	sions	32
R	efere	nces	34

#### Introduction

"Experience has taught me to be an optimist, at least in surface science"

— Sir John Brian Pendry

Self-assembly of organic and metal-organic compounds at surfaces has attracted a lot of attention in the past twenty years as a bottom-up approach for synthesizing nanoscale architectures. Since the time when the first studies on self-assembled monolayers (SAMs) were done, surface science researchers have tried multiple two-dimensional supramolecular assemblies at surfaces [1–8] and even made a prominent step in the field of on-surface synthesis [9–11]. To efficiently design and implement 2D networks, there are a few general categories of parameters that can be varied and controlled. They are the choice of the precursor and substrate, the utilization of metal adatoms, the growth process control, the regulation of the environment, and activation-method selection. Having control over all the parameters and possessing an appropriate theory give one the ultimate possibility to predict and create the desired final structure.

Along with the plethora of tested molecular precursors, substrates, adatoms, growth, and environment parameters, different approaches to initiate on-surface reactions have been investigated. In general, four main ways to bring energy into the system and induce transformations have been demonstrated so far. The most common, and probably the simplest one is thermal activation. Temperature tuning allows control over the reaction energy profile of the system, which means that kinetically trapped and equilibrium structures can be created selectively [12]. In the area of on-surface synthesis, thermal activation usually plays a crucial role, providing, in some cases, reaction specificity [11]. Despite the attractiveness of this approach, it has weak spatial localization and kinetic control. Among the alternative approaches to supply energy into the system, the best known are the injection of electrons generated by the tip of a scanning tunneling microscope (STM), light and electron beam irradiation. Compared to thermal annealing, these methods are more flexible in terms of controlling the kinetics of on-surface processes and can be used to deliberately switch between different types of rate-limiting mechanisms, e.g., from diffusion to reaction limited. Besides, the nature of these methods implies their application on small sample areas, which brings excellent spatial localization.

This thesis is dedicated to the self-assembly of 4,4'-biphenyldicarboxylic acid (BDA) on silver substrates and attempts, first of all, to answer the following questions: (i) how does BDA self-assembly proceed in diffusion-limited conditions? (ii) what role does the surface-plane orientation of the substrate play in the self-assembly? and (iii) how does the non-thermal activation by low-energy electrons influence the kinetics of the self-assembly? Based on the questions posed, the thesis has been organized into five chapters.

Chapter 1 is dedicated to the general questions of molecular self-assembly. We begin with the common definition of this phenomenon as a thermodynamic process and demonstrate that its nature is usually more complex than described in the definition. In particular, it is discussed that each molecular self-assembly is an intricate game between thermodynamic stimuli and kinetic restrictions. We briefly classify the main self-assembly pathways with respect to the role that kinetics play in their evolution. Further, the story switches to molecular self-assembly on surfaces, considering the main features specific to systems on surfaces. After discussing the general concepts, we dive into a more detailed theoretical description of the thermodynamic and kinetic aspects of molecular self-assembly on surfaces. The final part of Chapter 1 addresses the interaction of the electron beam with molecules. This part is important for our later discussion on the non-thermal activation of surface processes. Chapter 2 touches upon the experimental methods employed in the research work presented in the thesis. We describe the instrumentation cluster where the work has been done and bring a brief specification of the used measurement tools. Chapter 3 deals with the self-assembly of BDA on Ag(001) in diffusion-limited conditions. To create such conditions, we have used BDA coverages close to a complete monolayer (i.e., when the substrate surface is fully covered by a single layer of molecules). We also bring a concise description of BDA self-assembly on Ag(001) at submonolayer coverage to compare the full-layer and submonolayer assemblies. To reveal the role of surface-plane orientation in molecular self-assembly on surfaces, we put a comparative study of BDA self-assembly on Ag(001) and Ag(111) on the table in Chapter 4. We conclude the thesis by Chapter 5, discussing the possibility of activating on-surface processes non-thermally. Non-thermal activation allows tuning the temperature-dependent rate hierarchy, i.e., the rate of a specific process can be changed without affecting the rates of other temperature-dependent processes. In this chapter, we describe the deprotonation reaction of BDA on Ag substrates induced by low-energy electron irradiation. The deprotonation is the driving force of BDA phase transformations and plays a crucial role in BDA self-assembly.

### 1. Molecular self-assembly

The term self-assembly is applied to multiple phenomena around us and, in a broad sense, implies a process when constituents of a system arrange themselves into structured, ordered patterns. Self-assembly can be found everywhere at all scales. To give a few examples: the growth of atomic, ionic, molecular crystals [13, 14], complex protein folding [15], virus capsids [16] and bacterial colonies [17] organization, the collective behavior of animals [18, 19], the assembly of macro objects [20], stars formation [21] and many more. The scope of this thesis addresses the scale of self-assembly at atomic and molecular levels. At these levels, the principles of supramolecular chemistry can be adapted to create novel self-assembled functional materials with desired properties.

Molecular self-assembly is driven by thermodynamics, which brings a system from a disordered state to a more favorable (from the energetic point of view) ordered configuration since assembled structures usually have lower free energy than their separated constituents. However, self-assembly is a non-equilibrium process and does not ensure that the system will get to the equilibrium state. Quite often, self-assembly leads to the formation of thermodynamically metastable structures, that is, structures being in a local free energy minimum distinct from the global minimum. In some cases, the resulting structure does not even arrive at a local minimum and stays ordered in this high-energy state for a time exceeding the experimental observation time.

For further discussion, we need to make a distinction between near-equilibrium and far-from-equilibrium self-assembly. The former process implies that thermodynamic motifs are dominant in the formation of a new structure, whereas the latter points out the prevalence of kinetic factors. In reality, both mechanisms can be present and the balance between them defines the outcome. Experiments and computer simulations confirm that successful self-assembly commonly requires subtle balancing between thermodynamic stimuli for a system to decrease its free energy and the ability of components to move freely to achieve the resulting ordered configuration [22].

Figure 1.1 demonstrates the discussed balancing principle. To design a thermodynamically stable structure, binding between molecules has to be strong enough to decrease the total free energy of the assembled system (Figure 1.1d). If this condition is not fulfilled, the encountering of two or more molecules does not lead to a bond formation. At the same time, the binding has to be specific to make the desired structure more energetically favorable than other possible configurations. If this is not the case, an alternative structure distinct from the target structure can form (Figure 1.1f). The specificity can be implemented via directional binding, e.g., using anisotropic molecular components, through selective binding or chemical complementarity [22]. On the other hand, if the interactions between molecules are too specific, self-assembly can not happen within reasonable time (Figure 1.1g). Therefore, the interactions have to be somewhat not so specific to provide

the possibility for the molecules to "stick" to each other and build ordered agglomerates. However, non-specificity causes structural defects in the resulting pattern imposing some restrictions on the binding strength. Indeed, to correct the defects, the binding must not be so strong, otherwise, the molecules will not be able to break the bonds and reassemble. If the binding is too strong, the defect-correction mechanism does not work and the resulting structure turned out to be kinetically trapped (Figure 1.1e). All the discussed limitations make the self-assembly of a thermodynamically stable system possible only in a narrow region of the parameters (Figure 1.1c). If the assembly proceeds in this region, then thermodynamic principles can be employed to understand and predict its output.

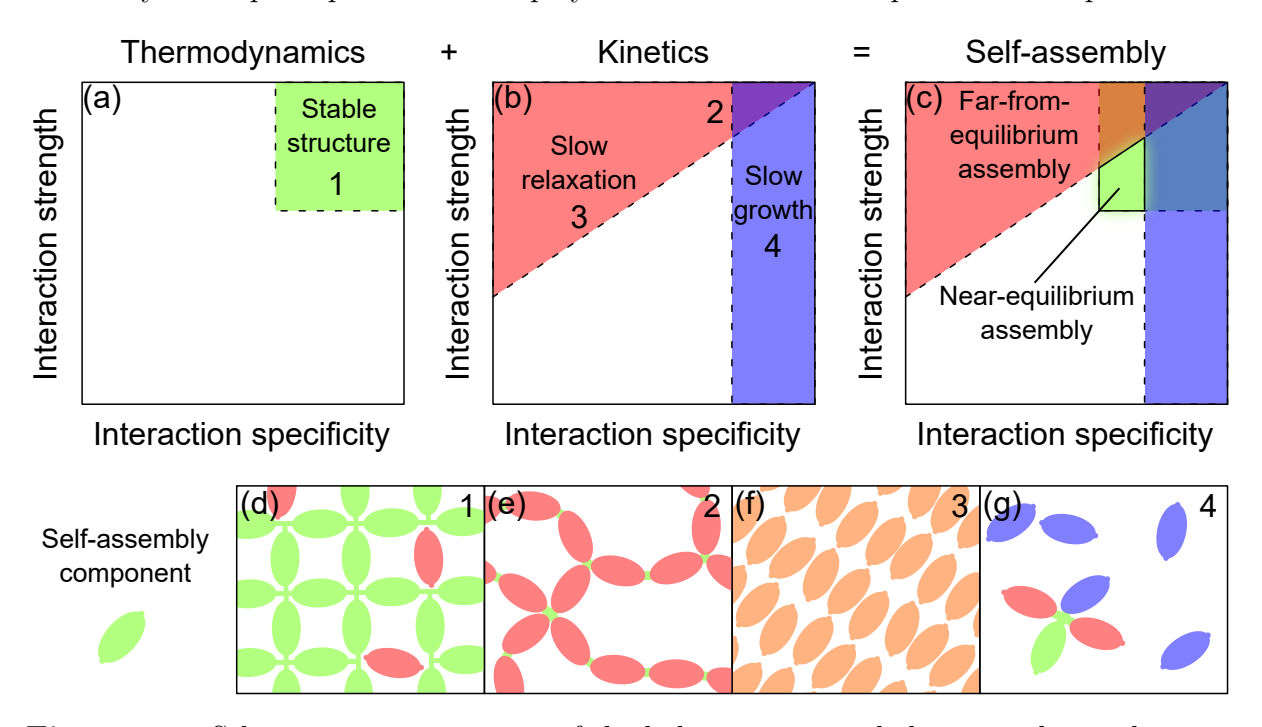


Figure 1.1: Schematic representation of the balancing principle between thermodynamic and kinetic aspects in a resulting structure. (a) A schematic phase diagram where self-assembly is governed by thermodynamics. (b) The interaction-parameter regions where kinetic processes prevail. (c) Only a small range of the parameters turns out to be suitable for near-equilibrium assembly. (d) A thermodynamically stable structure obtained with the parameters from region 1. (e) Too strong molecular interactions cause the formation of a kinetically trapped structure (region 2). (f) Weakly specific interactions lead to an alternative assembly with respect to the desired one (region 3). (g) Strong specificity hampers self-assembly (region 4). The color of the self-assembly components indicates their affiliation with the interaction types and subsequent formation of the resulting structure (e.g., the reddish components belong to molecules with excessively strong molecular interactions, which results in a kinetically trapped structure). The figure is adapted from [22].

Figure 1.2 depicts the formation of resulting phases from monomers through intermediate, metastable structures. Depending on parameters and environmental conditions, a system can assemble along different pathways, where the assembly evolution along a particular route is defined by the corresponding free-energy profile. We divide all the pathways into near-equilibrium (Figure 1.2a-c) and far-from-equilibrium (Figure 1.2d-f).

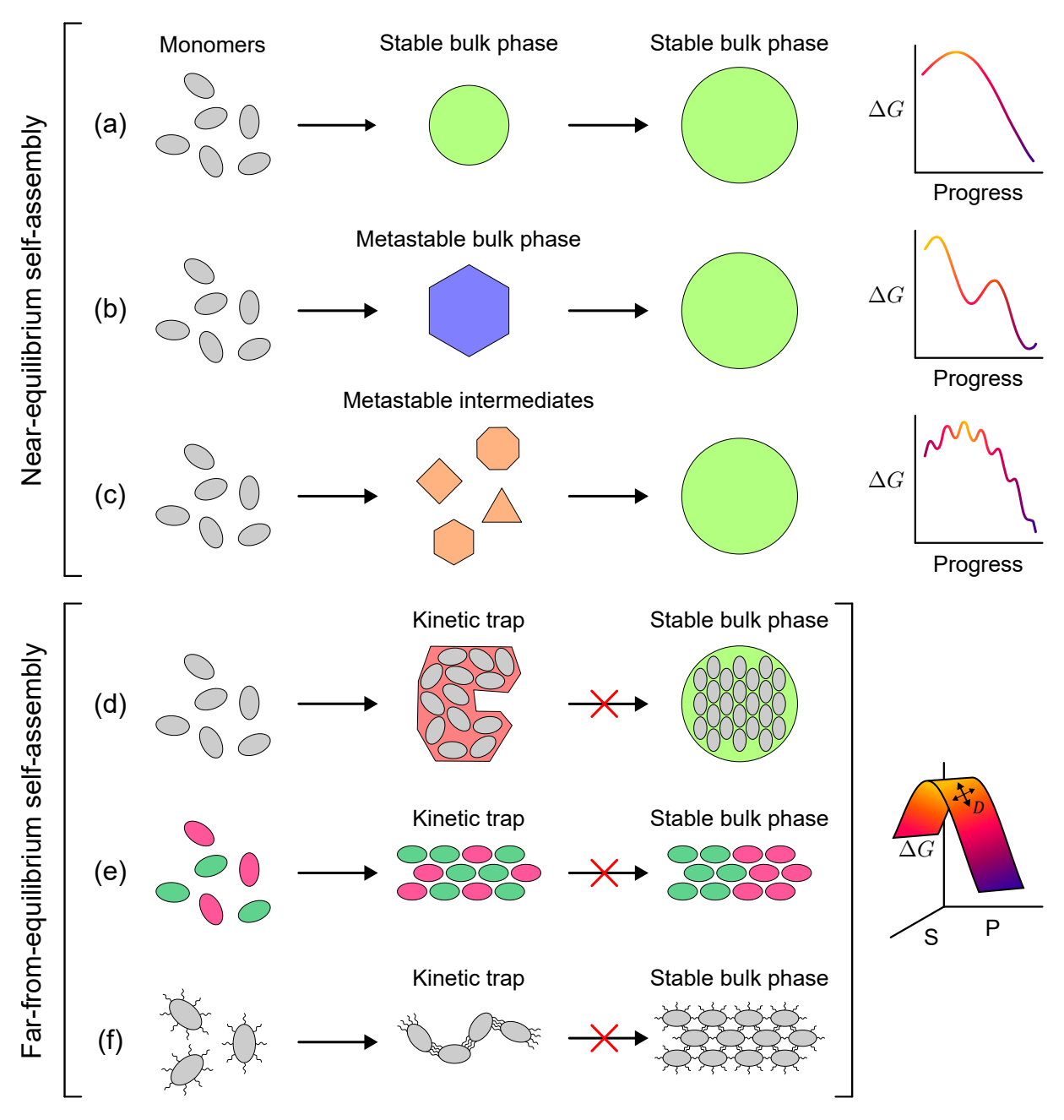


Figure 1.2: Schematic view of the main molecular self-assembly pathways. (a)-(c) Near-equilibrium assembly pathways. The corresponding free-energy profiles are shown on the right, where the axes denoted  $\Delta G$  and "Progress" mean the Gibbs free energy change and self-assembly reaction coordinate, respectively. (d)-(f) Far-from-equilibrium assembly pathways. A 3D chart with the free-energy surface and anisotropic diffusion tensor (D) is shown on the right. The diffusion tensor indicates the probable motion of the system on the energy surface due to competitive kinetic processes. The axes' notations are "Structure" and "Progress" for S and P, respectively. The description of the pathways is given in the text. The figure is adapted from [22].

Near-equilibrium routes can be predominantly described by thermodynamic principles and the kinetic component only serves to carry the system along the preferential trajectories on the free-energy surface. In the case of far-from-equilibrium routes, the kinetic effects start to play a crucial role and the development of self-assembly cannot be explained by purely thermodynamic assumptions. Since kinetics is defined by the microscopic behavior of assembling particles, there might be a competition between various kinetic processes leading to movement on the free-energy surface substantially impacted by kinetic phenomena.

If we now consider the growth of self-assembled molecular structures on a surface in ultra-high vacuum (UHV) conditions, which are the experimental conditions of the work presented in this thesis, we have to take into account the processes emerging when molecules are deposited on the surface. Among the processes, on-surface diffusion is of great interest to us since the ratio of diffusivity to deposition flux (D/F) defines either the self-assembly will be dominated by thermodynamic or kinetic motifs [23]. It is important to note that we apply the term self-assembly to both thermodynamic and kinetic types of assemblies. However, there is a terminological distinction between them in literature. The former is usually titled "self-assembly", whereas "self-organization" is often used for the latter [24]. As we have seen before, almost any transition from a disordered state to an ordered structure is induced by a combination of thermodynamic and kinetic stimuli. Since self-assembly is regarded as a bottom-up method in this thesis, where the main purpose is to construct molecular architectures with desired properties (no matter if thermodynamically stable or kinetically trapped), we have decided not to use two different terms and apply rather one integrated to emphasize the complex nature of the pathways towards the resulting structure. Coming back to D/F, if the flux is high and the diffusivity is low, molecules are not able to reach their lowest possible energetic state and rather get trapped in a kinetically restricted state. On the contrary, if the diffusivity is high and the flux is low, molecules can easily move on the surface and have enough time to form the thermodynamically favorable structure. Although the concept of D/F is, in general, applicable to the description of molecular systems, one has to use it cautiously. This is because the D/F ratio comes from the theory of epitaxial growth, where the formation of thin films is normally considered for atomic systems.

In the case of molecules, if intermolecular interactions are too strong, the system can easily be kinetically blocked despite the high diffusivity. Such behavior indicates that molecular self-assembly on surfaces is governed by a subtle interplay between molecule-molecule and molecule-substrate interactions. The basic molecule-molecule interactions with their lengths, strengths, and nature are given in Table 1.1. Due to its selectivity

**Table 1.1:** Basic on-surface intermolecular interactions with their characteristic strength, bonding length and nature. The table is adapted from [23].

Interaction type	Strength	Bonding length	Nature
van-der-Waals	$\sim 0.1 \text{ eV}$	0.5 1 nm	non-selective
H bonding	$0.1\\ 0.5\ \mathrm{eV}$	$0.20~\dots~0.35~\mathrm{nm}$	selective, directed
Electrostatic	$0.1\\ 3\ \mathrm{eV}$	up to several nm	non-selective
Dipole-dipole	$0.1\\ 0.5\ \mathrm{eV}$	$0.2 \dots 0.3 \text{ nm}$	directed
Metal complexation	$1 \dots 3 \text{ eV}$	$0.2 \dots 0.3 \text{ nm}$	selective
Substrate-mediated	$0.1 \ \ 1 \ \mathrm{eV}$	up to $7 \text{ nm}$	oscillatory
Reconstruction mediated	1  eV	system dependent	covalent

and directionality, hydrogen bonding is probably the most common type of interaction employed to build on-surface self-assembled networks [25, 26]. In our work, we have utilized BDA, which is a famous model molecule having carboxyl functional groups and able to form periodic structures based on hydrogen bonds [27, 28]. The discussion above puts an accent on the complexity of the self-assembly phenomenon. Since it consists of thermodynamic and kinetic components, it is worth providing a more detailed description of those.

#### 1.1. Thermodynamics and kinetics of molecular selfassembly on surfaces

Molecular self-assembly on surfaces is often a first-order phase transition, which includes new-phase nucleation and growth. Nucleation has always attracted a lot of attention and has been studied in diverse scientific fields [29–32]. To understand and predict the result of this intricate phenomenon and, therefore, the result of the corresponding self-assembly, one has to investigate the thermodynamic driving motifs and how these motifs can be influenced by the microscopic (i.e., kinetic) behavior of the system. This section considers the main theoretical approaches developed to describe the thermodynamics and kinetics of nucleation and growth in on-surface molecular self-assembled systems.

## 1.1.1. Thermodynamic aspects of nucleation and growth in self-assembled molecular systems on surfaces

The nucleation process usually requires the formation of small agglomerates, which represent seeds of a new phase (assuming that the structures of nuclei and large islands in the new phase are identical) in the environment of the old one. These agglomerates are metastable entities, and their appearance and disappearance are governed by statistical fluctuations. When the size of such an agglomerate reaches the so-called critical nucleus size, the probability of the disappearance drops substantially, and the new phase can grow. Thermodynamically, the growth of a new-phase nucleus consisting of j particles is defined by a free energy change  $\Delta G$  and expressed as follows:

$$\Delta G(j) = S(j)\gamma + j\Delta\mu \tag{1.1}$$

where  $\Delta \mu = \mu_2 - \mu_1$  is a difference between the chemical potentials of the new  $(\mu_2)$  and old  $(\mu_1)$  phases. If  $\mu_2 < \mu_1$ , the term  $\Delta \mu$  becomes negative, leading to a decrease in the free energy. The boundary (either area or length, depending on dimensionality) of a forming nucleus S(j) is proportional to  $\alpha j^{1-1/d}$ . Here,  $\alpha$  stands for a geometrical constant, and d means the dimension of the system. If the nucleus is in thermodynamic equilibrium, its shape can be described by the Wulff theorem [33].  $\gamma$  indicates the interface free energy between the old and new phases.

In Equation 1.1, the first term is typically positive giving rise to a nucleation barrier (Figure 1.3). The j corresponding to the maximum value of the barrier is called critical nucleus size and can be found by a solution of  $d(\Delta G)/dj = 0$  (in this case, the condition

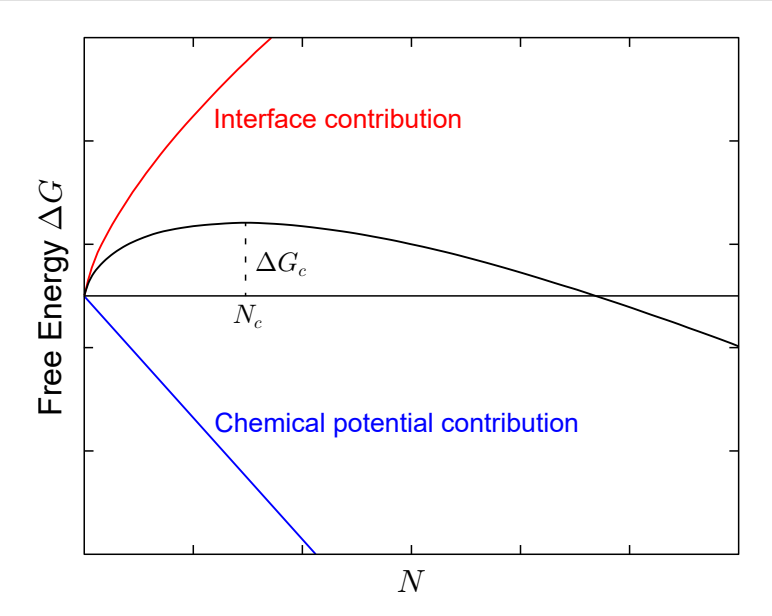


**Figure 1.3:** The nucleation barrier induced by the interplay between the interface free energy and chemical potential change. The figure is adapted from [34].

of the function's maximum):

$$i = \left[ \frac{(1 - 1/d)\alpha\gamma}{\Delta\mu} \right]^d. \tag{1.2}$$

The associated free energy, sometimes termed "activation Gibbs free energy", is then:

$$\Delta G_i = i \frac{\Delta \mu}{d-1} = \frac{\left[ (1 - 1/d)\alpha \gamma \right]^d}{(d-1)\Delta \mu^{d-1}}.$$
 (1.3)

As it has been mentioned above, the nucleation barrier imposes certain restrictions on the size of the agglomerates (clusters) to be stable. When j < i, the cluster very likely dissolves and is not able to initiate the growth of a new phase, whereas j > i leads to the formation of the new phase with a high probability. The Boltzmann factor  $\exp(-\Delta G/k_bT)$  defines the probability that the critical nucleus will appear. Since  $\Delta G_i \propto 1/\Delta \mu^{d-1}$ , a small  $\Delta \mu$  value causes a large nucleation barrier making the nucleation process highly improbable.

At the end of this subsection, we would like to note that the nucleation and growth are predominantly considered in the framework of kinetic processes. However, as demonstrated in [35], thermodynamics can also be reasonably applied at certain conditions, even for inorganic materials.

## 1.1.2. Kinetic aspects of nucleation and growth in self-assembled molecular systems on surfaces

Having a notion about the thermodynamic driving motifs, the next logical step is to identify the kinetics of the nucleation and growth. In this case, the kinetics, first of all, aims to predict the rate of nuclei formation, which is crucial for describing how a new phase appears and subsequently grows. There are two most popular theoretical approaches applied for the explanation of nuclei emergence. The first, so-called classical nucleation theory, relies on the assumption of a steady-state nucleation process, whereas the second

— rate equation theory — exploits differential equations to mathematically formulate the balance of elementary processes happening when a new phase appears. In this subsection, we will address the two theories in detail.

The classical nucleation theory goes back to the paper of Volmer and Weber [36]. In their work, the authors suggested the concept of the critical droplet (cluster) and the expression for the nucleation rate in a supersaturated vapor:

$$I \approx N_0 f_i^+ \exp\left(-\frac{\Delta G_i}{k_B T}\right) \tag{1.4}$$

where  $N_0$  is the number of corresponding nucleation sites and  $f_i^+$  is the attachment rate of monomers to the critical-size droplet.  $N_0 \exp\left(-\frac{\Delta G_i}{k_B T}\right)$  indicates the population of critical droplets at equilibrium. This relation was the first step toward the description of the nucleation process.

Later on, Farkas [37], Becker and Döring [38], Zeldovich [39], and Frenkel [40] developed what is now known as "classical nucleation theory" (CNT). Their main assumption was that droplets containing j monomers (atoms, molecules) increase and decrease in size by adding or losing a monomer. Mathematically, the time-dependent population of clusters  $(\Phi_j)$  can then be represented by a one-dimensional Markov chain as follows:

$$\Phi_{j-1} + \Phi_1 \xrightarrow{f_{j-1}^+} \Phi_j$$

$$\Phi_j + \Phi_1 \xrightarrow{f_{j+1}^+} \Phi_{j+1}.$$
(1.5)

 $f_j^+$  and  $f_j^-$  signify the attachment and detachment rates of single monomers, respectively. The interaction of clusters with dimers, trimers, and so on is considered to be much less frequent than with monomers and thus can be neglected.

A steady-state solution for the nucleation rate has been demonstrated by Becker and Döring in their famous work [38] and has become a synonym of CNT in literature. It is important to emphasize that Volmer and Weber have assumed the equilibrium size of the cluster, while Becker and Döring have discussed steady-state nucleation. The resulting solution is given by (for the derivation of the nucleation rate from classical nucleation theory, one can refer to [34] for example):

$$I = N_0 f_i^+ Z \exp\left(-\frac{\Delta G_i}{k_B T}\right). \tag{1.6}$$

Here, Z means the Zeldovich factor, which is determined by

$$Z \equiv \left(\frac{\eta}{2\pi k_b T}\right)^{1/2} \tag{1.7}$$

and

$$\eta = -\frac{\partial^2 \Delta G(j)}{\partial j^2} \bigg|_{j=i}. \tag{1.8}$$

The factor reflects the diffusive nature of nucleation dynamics and stands for the probability that a critical cluster will keep growing further and not dissolve. Considering the kinetic theory of surface diffusion and implying the same transition probability in each direction, the mean squared displacement of diffusing particles, based on random walk statistics, is given by  $\langle \Delta r^2 \rangle = 4Dt$  for 2D systems, where D and t are the diffusion coefficient and time, respectively. Since  $f_i^+ Z$  essentially determines the hopping rate leading to the nucleus formation, we can substitute the mean-squared-displacement equation with the relation for mean free path and mean free time:  $\lambda^2 = 4D\tau$ , with  $\lambda$  and  $\tau$  being mean free path and mean free time, respectively. Thus, the Zeldovich factor can also be expressed in terms of the diffusion coefficient:  $f_i^+ Z = 1/\tau = 4D/\lambda^2$ .

We now move to rate equation theory (RET), which was first introduced by Zinsmeister in his publications in the 1960s [41–44]. This discussion relies primarily on the work of J.W. Evans et al. [45], where a simplified version of the rate equations is considered. Despite the simplicity, this version is a good approximation and sufficient enough to get a notion about the kinetics of nucleation and growth. For a more detailed analysis, one is encouraged to address the papers of J. A. Venables [46–48], who also made a significant contribution to the development of the theory. As it is clear from its title, RET tends to describe single microscopic processes happening during the nucleation and growth as a system of differential equations. To write the system of equations in a simplified version, we need to make a few assumptions. We consider the on-surface nucleation and growth of a monolayer film under a flux of monomers (F) with such coverage of deposited material  $(\theta)$ when there is no coalescence between growing clusters yet, and the deposition of monomers on the top of existing clusters is negligible. We also assume complete condensation, i.e., there is no re-evaporation of deposited material (which is realistic for large molecules deposited on metal substrates at room temperature) and monomers being the only mobile objects on the surface. With the assumptions above, we can write:

$$\frac{\mathrm{d}N_1}{\mathrm{d}t} \approx F - (i+1)K_{nuc} - K_{agg} \tag{1.9}$$

$$\frac{\mathrm{d}N_j}{\mathrm{d}t} = K_{j-1} - K_j \quad (j \geqslant 2). \tag{1.10}$$

 $N_1$  and  $N_j$ , in this case, denote the number of monomers and agglomerates containing j constituents per unit area, respectively. The flux F, for an ideal gas at pressure p, can be estimated by  $p(2\pi mk_BT)^{-1/2}$  with m,  $k_B$  and T being molecular mass, the Boltzmann constant, and temperature, respectively or alternatively is provided by an evaporation source or incoming ions from a solution. i and t are critical nucleus size and time, respectively.  $K_{nuc}$  and  $K_{agg}$  indicate nucleation and aggregation rates, respectively.  $K_j$  is the net-capture rate of monomers by clusters of size j.

We can further simplify the kinetic equations by assuming that the emergence and disappearance of clusters with size  $j \leq i$  are in thermodynamic equilibrium and their density is given by the so-called Walton relation, which can be deduced from the detailed balance or a statistical mechanical approach [46, 49]:

$$N_{j} = (N_{1})^{j} \sum_{m} C_{j}(m) \exp[\beta E_{j}(m)]$$
(1.11)

with  $E_j(m)$  being the binding energy of m-type clusters with size j,  $C_j(m)$  being statistical weights dependent on the configurational and other contributions to the entropy of m-type

clusters with size j [48], and  $\beta = 1/(k_B T)$ . The thermodynamic-equilibrium assumption leads to  $dN_j/dt = 0$  for  $(2 \le j \le i)$ . If we now separate "subcritical"  $(j \le i)$  and stable (j > i) clusters and sum up the stable clusters:

$$N_s = \sum_{j=i+1}^{\infty} N_j \tag{1.12}$$

Equation 1.9 and Equation 1.10 turn into:

$$\frac{\mathrm{d}N_1}{\mathrm{d}t} \approx F - (i+1)K_{nuc} - K_{agg} \tag{1.13}$$

$$\frac{\mathrm{d}N_j}{\mathrm{d}t} = 0 \quad (2 \leqslant j \leqslant i) \tag{1.14}$$

$$\frac{\mathrm{d}N_s}{\mathrm{d}t} \approx K_{nuc}.\tag{1.15}$$

To solve the given system of equations, we need to define  $K_{nuc}$  and  $K_{agg}$  terms. To form a stable cluster, a critical agglomerate has to attach a monomer, which makes the nucleation rate  $K_{nuc}$  proportional to  $N_1N_i$  [48]:

$$K_{nuc} = \sigma_i h N_1 N_i \tag{1.16}$$

where h is the hopping rate determining the on-surface diffusion of monomers and described by the Arrhenius law  $\nu \exp(-\beta E_d)$ , with  $\nu$  and  $E_d$  being a prefactor and the diffusion barrier, respectively. The term  $\sigma$  specifies the so-called "capture number", which determines the diffusional flow of monomers towards critical  $(\sigma_i)$  or stable  $(\sigma_s)$  clusters from the surrounding area. The  $\sigma$  has been the subject of thorough research and can be defined as a solution to two-dimensional diffusion problems in the form of Bessel functions. As a rough guess, one can think of them as slowly varying values in the range 2–4 for  $\sigma_i$  and 5–10 for  $\sigma_s$ . For further information, the references [45, 47] can be addressed. If we assume a simplified Walton relation for  $N_i$ :

$$N_i \approx (N_1)^i C_i \exp[\beta E_i] \tag{1.17}$$

Equation 1.16 becomes:

$$K_{nuc} = \sigma_i h N_1 N_i = \sigma_i h C_i \left( N_1 \right)^{i+1} \exp[\beta E_i]. \tag{1.18}$$

The aggregation rate is defined in the same manner:

$$K_{aqq} = \sigma_s h N_1 N_s. (1.19)$$

With  $K_{nuc}$  and  $K_{agg}$  defined, we can move to the discussion of nucleation and growth regimes.

At the initial stage of deposition, when there is almost no adsorbed material, the nucleation of far-separated clusters happens. This is the so-called "transient" regime [47]. Each cluster has a depletion zone around it. If a monomer reaches the zone, it is considered

to be attached to the cluster. A solution of Equations 1.13–1.15 in the transient regime gives the following expression for the density of stable clusters:

$$N_s \approx (i+2)^{-1} \sigma_i C_i \left(\frac{h}{F}\right) \theta^{i+2} \exp[\beta E_i]$$
 (1.20)

where coverage  $\theta = Ft$ .

After a certain time, when the clusters are large enough, their depletion zones cover the surface completely. At this point, the system switches to the "steady-state" regime  $(dN_1/dt = 0)$ . The density of stable clusters in the "steady-state" regime is defined by:

$$N_s \approx \left( (i+2)\sigma_i \sigma_s^{-(i+1)} C_i \right)^{\frac{1}{(i+2)}} \left( \frac{h}{F} \right)^{-\frac{i}{(i+2)}} \theta^{\frac{1}{(i+2)}} \exp \left[ \frac{\beta E_i}{(i+2)} \right].$$
 (1.21)

The main feature of the above solutions (Equation 1.20 and Equation 1.21) is the  $N_s$  dependence on h/F. This ratio is central to the solutions family for the density of stable clusters at different regimes and is termed the scaling relation of nucleation. As we have discussed in Chapter 1, the scaling relation (instead of the hopping rate h, the equivalent diffusivity term D has been used in Chapter 1) turns out to be decisive for the evolution of a self-assembling system and, in general, determines if the system is able to reach the thermodynamic equilibrium or is kinetically trapped. By varying h/F, one can essentially control the process of self-assembly.

From Equation 1.20 and Equation 1.21, the crossover coverage  $(\theta^*)$ , where the transient regime switches to the steady-state one, can also be deduced:

$$\theta^* = (i+2)^{\frac{1}{(i+1)}} \left(\sigma_i \sigma_s C_i\right)^{-\frac{1}{(i+3)}} \left(\frac{h}{F}\right)^{-\frac{2}{(i+3)}} \exp\left[-\frac{\beta E_i}{(i+3)}\right]. \tag{1.22}$$

By applying Equation 1.22 to Equation 1.20, we can now write the dependencies of  $N_s$  on the *scaling relation* and exponential term in all the mentioned regimes:

$$N_s \sim \left(\frac{h}{F}\right) \theta^{i+2} \exp[\beta E_i]$$
 — transient regime (1.23)

$$N_s^* \sim \left(\frac{h}{F}\right)^{-\frac{(i+1)}{(i+3)}} \exp\left[\frac{\beta E_i}{(i+3)}\right]$$
 - crossover (1.24)

$$N_s \sim \left(\frac{h}{F}\right)^{-\frac{i}{(i+2)}} \theta^{\frac{1}{(i+2)}} \exp\left[\frac{\beta E_i}{(i+2)}\right]$$
 - steady-state regime. (1.25)

Finally, to complete the description of nucleation and growth, we need to consider the size distribution of the clusters. Taking into account the dynamic scaling assumption [50], the cluster-size distribution can be defined by the general scaling form [51]:

$$N_j(\theta) = \theta J^{-2} f_i(j/J) \tag{1.26}$$

where  $N_j(\theta)$  corresponds to the density (per site) of clusters with j constituents at  $\theta$  coverage.  $J(\theta) = \sum_j j N_j(\theta) / \sum_j N_j(\theta)$  is the average cluster size and  $f_i$  denotes the scaling function, which is being a probability distribution normalized based on  $\int_0^\infty f_i(u) du =$ 

 $\int_0^\infty f_i(u)u \, du = 1$ . The empirical relation for the scaling function with respect to u and the critical-nucleus size i has been derived by J. G. Amar et al. [51] in their work on the Monte Carlo simulations of epitaxial growth:

$$f_i(u) = C_i u^i \exp^{-ia_i u^{1/a_i}} (1.27)$$

with the constants  $C_i$  and  $a_i$  given by:

$$\frac{\Gamma[(i+2)a_i]}{\Gamma[(i+1)a_i]} = (ia_i)_i^a, \quad C_i = \frac{(ia_i)^{(i+1)a_i}}{a_i\Gamma[(i+1)a_i]}$$
(1.28)

where  $\Gamma$  is the gamma function. These relations can be calculated from the normalization integral defined above.

Although the discussed thermodynamic and kinetic principles have been developed rather for atomic systems, they, in general, remain valid for molecular self-assembly on surfaces. A few additional aspects need to be paid attention to when considering molecular constituents instead of atomic ones. For example, geometric properties of molecules can play a significant role in the nucleation process, providing the possibility for several apparent activation energies [52]. Another important feature is the mutual arrangement of molecules with respect to the substrate, i.e., molecules can be "standing up" or "laying down" having various angles between the molecule and substrate. Despite these features, the general considerations developed for the thermodynamic and kinetic aspects of nucleation and growth work well for molecular systems too, and, therefore, can serve as a good theoretical means to describe and explain the phenomenon of on-surface molecular self-assembly.

## 1.2. The electron beam as a non-thermal activation tool of on-surface reactions

The concluding section of this chapter is dedicated to the discussion of low-energy electrons as a means to induce diverse chemical reactions. In particular, we consider the interaction of irradiating electrons with molecules being in the gas phase, agglomerated in clusters, and condensed on surfaces. We also discuss the chemical transformations of the molecules induced by that interaction. The relevance of this topic to molecular self-assembly becomes obvious if one recognizes in electrons a tool to non-thermally change the chemical composition of a self-assembled system. Such modifications can lead to surprising structures, sometimes unattainable by thermal annealing.

#### 1.2.1. Electron-molecule interaction

Electron-molecule interaction can lead to the dissociation of molecules through direct inelastic collisions. There are three channels in which the dissociation can occur: (i) electron impact ionization, (ii) electron impact excitation, and (iii) dissociative electron attachment (DEA). The corresponding channel is mostly defined by the primary electron energy and molecular phase.

Electron impact ionization is a direct non-resonant scattering phenomenon taking place when the energy of irradiating electrons surpasses the ionization potential of the exposed molecular species ( $\sim 10$  eV). The ionization cross section gradually increases with increasing electron energy and reaches a maximum at  $\sim 100$  eV. The duration of this process is  $\sim 10^{-16}$  s, that is, the time needed for the electron to traverse the molecule. Electron impact ionization leads to the formation of excited state cations AB<sup>+\*</sup> out of neutral species AB in the following way:

$$AB + e^{-} \rightarrow AB^{+*} + 2e^{-}$$
 (1.29)

which can then result in the dissociation of the cation:

$$AB^{+*} \to A \bullet + B^{+*} \tag{1.30}$$

with A• being a radical fragment. Alternatively, it can promote reactions between the cation and surrounding molecules or electron-ion recombination [53].

Electron impact excitation is also a direct non-resonant short-lived scattering process. For small molecules, it starts at  $\sim$ 6–8 eV, and its cross-section reaches a maximum at  $\sim$ 40–60 eV. We can write the following general expression for electron impact excitation:

$$AB + e^{-} \rightarrow AB^{*} + e^{-}$$
 (1.31)

where AB\* is the pristine molecule in an electronically excited state. There are three contending ways of decaying the excited molecule. The first way implies the emission of a photon or the dissipation of energy via non-radiative interaction with surroundings:

$$AB^* \to AB + E \tag{1.32}$$

where E indicates the dissipated energy. The second and third channels assume the decomposition of the excited molecule into neutral radicals and ion pairs, respectively:

$$AB^* \to \bullet A^* + B \bullet \tag{1.33}$$

$$AB^* \to A^+ + B^-.$$
 (1.34)

To provide the description of the last dissociative channel, which is dissociative electron attachment or sometimes just dissociative attachment, we first need to introduce the step preceding the decomposition. This step is the formation of the so-called transient negative ion (TNI). The TNI appears as a result of a Franck–Condon transition from the electronic ground state of a neutral molecule to either an electronically excited or ground state anion due to the electron attachment:

$$AB + e^- \rightarrow AB^- \text{ or } AB^{-*}$$
 (1.35)

where \* means electronic excitation. Since the energy of incident electrons has to fulfill the requirements of the Franck-Condon transition, the formation of the TNI is resonant in nature<sup>1</sup>.

In Figure 1.4, we demonstrate the classification of TNIs. In general, there are two main groups of TNIs: single-particle and core-excited resonances. The single-particle resonance appears at low energies ( $\sim 0-5$  eV) when an incoming electron attaches to a

<sup>&</sup>lt;sup>1</sup>For that reason, the TNI is sometimes called negative ion resonance.

molecule without its electronic excitation (single-particle process). In contrast, the electron attachment at higher energies ( $\sim$ 5–15 eV) can be accompanied by molecular electronic excitation; the resonance is then called core-excited resonance. TNIs can be further divided based on the energy of the TNI with respect to the energy of the neutral reference molecule. The neutral reference molecule is a molecule that has the same electronic configuration as the TNI but without the extra attached electron. If the TNI has higher energy than the reference molecule, the resonance is termed shape resonance; otherwise, it is termed Feshbach resonance (Figure 1.4).

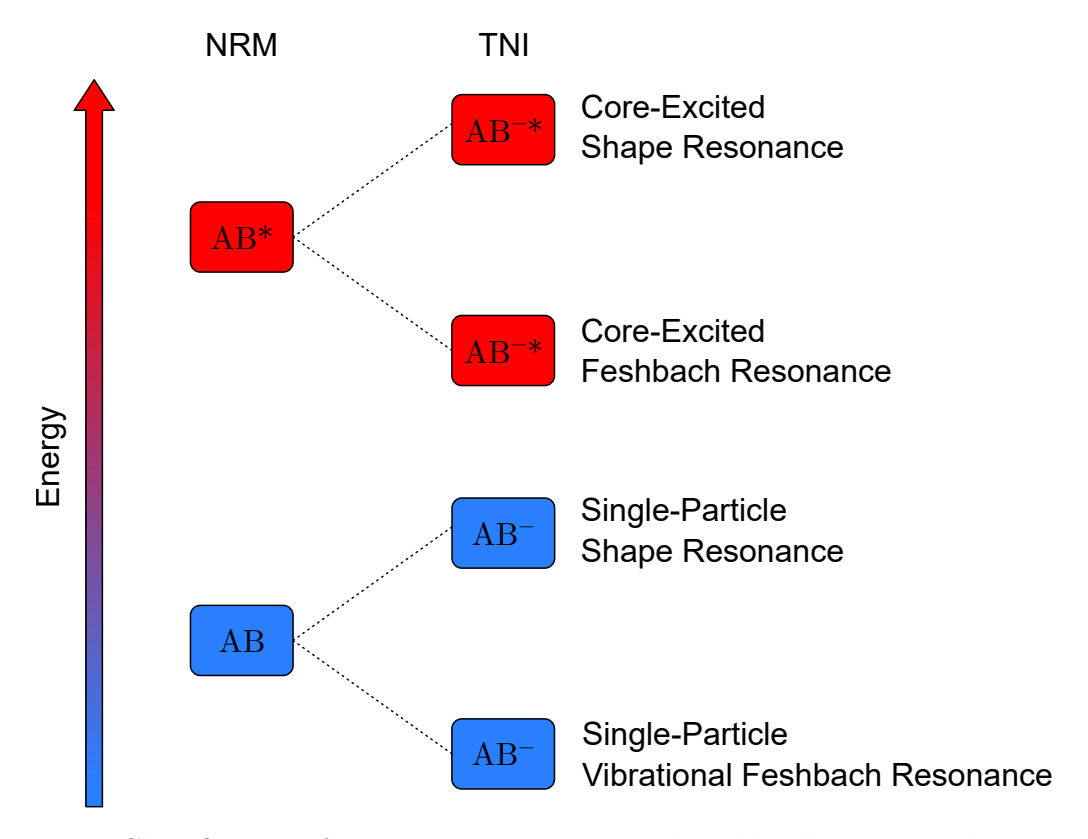


**Figure 1.4:** Classification of transient negative ions induced by electron attachment. NRM and TNI indicate the neutral reference molecule and transient negative ion, respectively. The figure is adapted from [53].

Having an idea of how TNIs form and are classified, we now return to the discussion of dissociative electron attachment along with other TNI relaxation channels. Despite the way how a TNI has been created, it always decays in one of four possible channels. Those channels can be divided into associative (without breaking apart the parent molecule) and dissociative relaxation channels. The associative channels include (i) autodetachment, (ii) radiative cooling (relaxation), and (iii), if the molecule is in the cluster or condensed state, associative attachment. The only dissociative channel is DEA. Further, we discuss the channels in detail.

If the lifetime of a resonance is shorter than the vibrational period of the nuclei, the TNI can relax into the neutral ground state of the parent molecule via autodetachment:

$$AB^{-*} \text{ or } AB^{-} \to AB + e^{-}$$
 (1.36)

Autodetachment can also leave the molecule in an excited state, e.g., rotationally, vibra-

tionally, and/or electronically excited:

$$AB^{-*} \to AB^* + e^-.$$
 (1.37)

Autodetachment lifetimes vary in a broad range from  $\sim 10^{-14}$  to  $\sim 10^{-3}$  s depending on the molecule identity. Complex molecules usually have long autodetacment lifetimes.

The second associative channel — radiative cooling — involves the emission of a photon and, subsequently, the formation of a stable ion:

$$AB^{-*} \to AB^{-} + h\nu. \tag{1.38}$$

This type of relaxation is only available for molecules with positive adiabatic electron affinity, that is, when the ground state of the anion is energetically lower than the ground state of the precursor molecule. Besides, it typically has a much longer lifetime ( $\sim 10^{-8}$  s) compared to that of autodetachment ( $\sim 10^{-13}$  s). For this reason, radiative cooling is often treated as the least probable (non-competitive) decay channel of TNIs. The last associative channel (associative attachment) will be discussed later when we consider the behavior of the TNI in the condensed state.

We now move to the discussion of the dissociative relaxation channel — DEA. Autodetachment and DEA have comparable lifetimes, and, in this regard, the particular decay channel of the TNI is defined by the process that is faster. For the TNI to decompose through DEA, three conditions have to be fulfilled: (i) the resonance lifetime has to be relatively long ( $\sim 10^{-12}$ – $10^{-14}$  s), (ii) the TNI must be dissociative in the Franck–Condon region, and (iii) one of the resulting fragments should possess a positive electron affinity. If all the requirements are met, the decomposition of a simple diatomic molecule can take place in the following form:

$$AB^{-*} \to A \bullet + B^{-} \tag{1.39}$$

where the bond scission occurs along the A - B coordinate.

The cross-section of DEA can be calculated from  $\sigma_{DEA} = \sigma_0 P_{diss}$ , where  $\sigma_0$  is the cross-section of incident-electron attachment and  $P_{diss}$  is the probability of molecular dissociation. At very low energies, we can apply the Wigner threshold law [54] to find out the energy-dependent  $\sigma_0$ :

$$\sigma_0(E, l) \sim E^{l-1/2} \quad (E \to 0)$$
 (1.40)

with l being angular momentum. The dissociation probability  $P_{diss}$  is defined by the ratio of DEA and autodetachment lifetimes:  $\exp(-\tau_{DEA}/\tau_{AD})$ . Thus, the resulting relation for  $\sigma_{DEA}$  is expressed by:

$$\sigma_{DEA} = \sigma_0 \exp(-\tau_{DEA}/\tau_{AD}). \tag{1.41}$$

 $\tau_{AD}$  and  $\tau_{DEA}$  can be determined from the energy width of the TNI state via the Heisenberg uncertainty principle  $\Gamma \approx h/\tau_{AD}$  and the radial velocity v(R') of the emerging molecular fragments  $\tau_{DEA} = \int_R^{R_c} 1/v(R') \mathrm{d}R'$ , respectively. Here, R means the bond distance where the Franck–Condon transition happens, and  $R_c$  indicates the crossing point. Before  $R_c$ , the TNI can decay through the competing-to-DEA autodetachment process; after  $R_c$ , autodetachment is not possible.

When the TNI forms in a cluster, its negative charge induces polarization of the environment. The polarization process consists of two parts: (i) fast electron polarization, which proceeds on the time scale of the electron attachment, and (ii) the relatively

slow ( $\sim 10^{-12}$ – $10^{-10}$  s) rearrangement of the molecules to acquire the optimal state. The polarized environment stabilizes the TNI such that it usually has lower energy with respect to the neutral precursor. This applies to both single-particle and core-excited TNIs. Furthermore, a core-excited anion experiences an even stronger stabilization effect due to its higher polarizability.

Inelastic scattering processes in clusters also have a substantial influence on the formation of the TNI. The typical scattering process proceeds in two stages. First, an incoming electron interacts with a molecule causing a short-living core-excited shape resonance. The resonance decays by autodetachment, where the electron loses almost all its energy, and the molecule stays electronically excited. In the second stage, the slowed-down electron can attach to another molecule via a low-energy single-particle resonance. The newly formed TNI can further relax in two ways. The first way involves stabilization by the dissipation of the excessive energy in the surrounding environment (this is so-called associative attachment, as we mentioned previously in the text). The second way leads to TNI dissociation and the emergence of a stable anion fragment. The latter is possible only if the energy of the TNI is sufficient. Incoming electrons can also lose their energy through non-resonant inelastic processes; however, the efficiency of such processes is much lower.

Molecules in the condensed state do not differ much from those in the cluster form, and the phenomena observable for the interactions of low-energy electrons with molecules in clusters also apply to the interactions with condensed-state molecules. If we examine electron attachment to a molecule in the condensed state, we will discover that the possible outputs of this process can be boiled down to the following reactions:

$$AB_{ads} + e^- \rightarrow AB_{ads}^{-*}$$
 (1.42)

$$\rightarrow AB_{ads}^-$$
 (1.43)

$$\rightarrow A_{ads} \bullet + B_{ads}^{-} \tag{1.44}$$

$$\rightarrow A_{ads} \bullet + B^-$$
 (1.46)

where the subscript "ads" points out the condensed (adsorbed) state of the molecule. The yield ratios of Equations 1.44–1.46 depend on the spatial arrangement of the fragment on the substrate. Upright-standing fragments have the highest probability to desorb from the surface, whereas the fragments aligned with the surface have the lowest one. Besides, the outputs of Equations 1.45–1.46 are heavily affected by the underlying DEA processes (in particular energy losses) since the escaping fragments have to have enough kinetic energy to surmount the energy barrier due to the polarization of the substrate and surrounding molecules.

Furthermore, aside from the DEA processes, the TNI in the condensed state can decay through the interaction with the substrate and/or other constituents of the condensed phase. This channel can lead to the formation of a stable ion on the surface (Equation 1.43), which in turn, together with Equations 1.44–1.45, can result in the charging of the molecular film.

### 2. Experimental methods

This chapter provides an overview of the experimental methods used for the sample preparation and characterization in this thesis. In order to investigate atomic-scale phenomena, tight control of the experimental environment is necessary. In this work, we conducted all the experiments in ultra-high vacuum (UHV) conditions, which prevented contaminations of the studied systems. Substrates for our samples were cleaned by repetitive cycles of ion sputtering and thermal annealing. To prepare the samples, we used organic molecular beam epitaxy (OMBE). OMBE is considered a reliable tool for creating nanoscale architectures with high accuracy. The characterization part was carried out by surface science analytical techniques. In particular, we applied scanning tunneling microscopy (STM), low-energy electron microscopy/diffraction (LEEM/LEED), and X-ray photoelectron spectroscopy (XPS). Below, one will find a detailed description of the mentioned techniques and corresponding instrumentation.

#### 2.1. UHV cluster and sample preparation

All the experiments presented in this work were carried out with the use of the so-called UHV cluster. This facility belongs to CEITEC Nano Research Infrastructure and represents a unique complex of nine chambers connected by an elongated, pipe-like transfer line (TL). All the chambers, including TL, are held at a base pressure  $\sim 2 \times 10^{-8}$  Pa. We used Ag(100) and Ag(111) single crystals supplied by MaTeck and/or Surface preparation laboratory (SPL) companies as the substrates for our samples. The preparation of the substrates for subsequent OMBE was conducted in the so-called Preparation chamber intended for cleaning procedures and equipped with tools for ion sputtering and thermal annealing. Usually, we performed a few sputtering and annealing cycles before moving the crystals to the OMBE chamber. To prepare the samples involving the synthesis of self-assembled molecular networks, we used an oil-heated effusion cell and a four-pocket evaporator acquired from CreaTec Fischer & Co. GmbH and Dr. Eberl MBE-Komponenten GmbH, respectively. To estimate coverage after the molecular depositions, we applied LEEM and/or XPS. The molecules utilized as the building blocks for the self-assembled structures were purchased from Sigma-Aldrich Chemie GmbH.

#### 2.2. Scanning tunneling microscopy

The STM characterization of the samples prepared in this study was carried out with an Aarhus 150 variable-temperature SPM provided by SPECS Surface Nano Analysis GmbH.

The microscope allows conducting measurements in the range of -183–127 °C. All the STM data demonstrated in this work were collected at room temperature. As the tips for STM, we used regular etched tungsten tips and the so-called Kolibri sensors provided by SPECS. In addition to the tunneling current detection, the Kolibri sensor gives the possibility to conduct atomic-force-microscopy measurements [55]. The SPM chamber is equipped with an ion sputtering gun for tip preparation, and sputtering procedures were applied from time to time to keep the tips clean and sharp. The experimental data post-processing predominantly included drift correction based on the method described in [56].

#### 2.3. X-ray photoelectron spectroscopy

We conducted the XPS characterization of our samples at Materials Science Beamline of Elettra – Sincrotrone Trieste S.C.p.A. facility and on a home XPS set-up. The home set-up has an X-ray source with Al and Mg anodes, which produce  $K\alpha$  spectral lines with energies of 1487.6 eV and 1253.6 eV, respectively. The XPS analyzer used in the set-up is a Phoibos 150 analyzer from the SPECS Surface Nano Analysis GmbH company. It possesses a microchannel plate detector and a CCD camera. Additionally, our spectroscopic system provides the possibility to cool down and anneal samples in a 5-axis sample manipulator. A type K thermocouple was applied for temperature reading. We carried out the majority of the XPS measurements shown in this thesis at room temperature, although some investigations, where it was needed, included low-temperature XPS characterization.

#### 2.4. Low-energy electron microscopy/diffraction

In our work, we performed LEEM/LEED measurements on an FE-LEEM P90 apparatus supplied by SPECS GmbH. Generally, FE-LEEM P90 consists of illumination and imaging columns, a magnetic prism array, and an objective compartment. The illumination column forms a beam of emitted electrons and contains a system of lenses, deflectors, and a stigmator. The imaging column creates an image of the sample surface and transfers it onto a detector. It includes a system of projector lenses, deflectors, a prism deflector, and a detector system. The detector usually contains a multichannel plate and a fluorescent screen filmed by a high-resolution CCD camera. The magnetic prism array separates and deflects the incoming to and reflected from the sample electron beams. It consists of multiple electromagnetic coils, which fulfill the functionality of magnetic field segments. The objective compartment produces a decelerated electron beam interacting with the sample surface and accelerates the reflected electrons. It contains the transfer and objective lenses. FE-LEEM P90 also has a set of apertures. The microdiffraction aperture located at the upper diagonal of the prism allows one to restrict the irradiated surface up to 185 nm and, thus, get a diffraction pattern from the local, restricted area. The contrast aperture is placed in the exit plane of the prism. It limits the acceptance angle from the sample and partially removes spherical aberrations, leading to an increased image resolution. By choosing certain diffraction spots in the reciprocal space, the contrast aperture also allows for conducting dark-field-microscopy measurements. The selected area aperture is used to adjust the size of the e-beam leaving the prism.

# 3. On-surface molecular self-assembly at high coverage

Coverage is one of the main parameters that play a substantial role in molecular self-assembly on surfaces. Many studies are conducted at coverages lower than a monolayer (here, the monolayer means the coverage when the substrate surface is fully covered by a single layer of molecules). However, the structure of on-surface self-assembled systems at low coverage can differ significantly from those at high coverage.

In this chapter, we describe the self-assembly of a complete BDA monolayer on a Ag(100) crystal. Since effective BDA diffusion happens only in places where the surface is free of molecules, a complete monolayer causes the restriction of BDA surface diffusion. This leads to self-assembly in diffusion-limited conditions. BDA self-assembly at full-layer and submonolayer coverages have certain differences, and before we move to the description of BDA self-assembly at a complete monolayer, we should briefly discuss BDA self-assembly at submonolayer coverage.

# 3.1. Self-assembly of BDA on Ag(001) at submonolayer coverage

We chose 4,4 -biphenyl dicarboxylic acid as the model "building block" for our self-assembly experiments. It is known that BDA can form numerous self-assembled phases on various substrates [27, 28, 57–59]. The pristine BDA molecule consists of two phenyl rings and two functional carboxyl groups. Its structural formula is depicted in Figure 3.1.

Figure 3.1: The structural formula of BDA.

When deposited on Ag(001), BDA molecules adopt a planar configuration and self-assemble into molecular chains connected by hydrogen bonding between adjacent carboxyl groups. The substrate-molecule interactions are based on the van-der-Waals forces. If thermal annealing is applied, BDA carboxyl groups can lose hydrogen atoms or, in other words, deprotonate. The deprotonation leads to various ratios of protonated (2H-BDA), semi-deprotonated (1H-BDA), and fully deprotonated (0H-BDA) BDA molecules, which

in turn causes structural rearrangements of the molecules and the formation of new self-assembled structures. In total, we have discovered four main structures. We term them  $\alpha$ ,  $\beta$ ,  $\gamma$ , and  $\delta$  phases, where the as-deposited  $\alpha$  phase contains only 2H-BDAs,  $\beta$  and  $\gamma$  have certain ratios of 2H-BDAs, 1H-BDAs, and 0H-BDAs, and  $\delta$  involves only 0H-BDA molecules. The structural and chemical features, models, and formation temperatures of the phases are demonstrated in a summarizing Figure 3.3.

Among the phases, the most intriguing one is  $\alpha$  (Figure 3.3a,e,i,m) since it does not have a periodic structure. The only stable repeating features in the structure of the  $\alpha$  phase are BDA dimers and interchain periodicity. The diffraction spots corresponding to the dimers and interchain periodicity are marked by arrows and circles in Figure 3.3a, respectively. Due to the variable length of hydrogen bonds between adjacent molecules within a chain, there is no intrachain periodicity. In addition, there are two energetically equivalent positions of BDA molecules in neighboring molecular chains. This causes the formation of two spatial arrangements represented as tiles in Figure 3.3e,i. The variable lengths of the hydrogen bonds and the positional variation create the inherent disorder of the  $\alpha$  phase (more information is given in the following publication in this chapter).

When — due to the deprotonation — the fraction of deprotonated carboxyl groups (carboxylates) approaches 50 %,  $\alpha$  transforms into the  $\beta$  phase (Figure 3.3b,f,j,n).  $\beta$  has a structural unit cell but does not have regularity in chemical composition, i.e., the number of 2H-BDAs, 1H-BDAs, and 0H-BDAs present within a cell can change from cell to cell. The  $\beta$  phase demonstrates an interlocked row structure (Figure 3.3f) with the main binding motif being carboxylate—carboxyl hydrogen bonding; the remaining carbonyl-oxygen atoms mediate interchain connections. Since deprotonated carboxyl groups interact with the substrate stronger than non-deprotonated ones, the structure of the  $\beta$  phase is modulated by Ag(001) more than the structure of  $\alpha$ . This leads to the  $\beta$  phase being commensurate with the substrate unit cells. The commensurability manifests itself in a moiré pattern with a much larger periodicity than the unit cell of  $\beta$  [27].

If the deprotonation continues, the  $\gamma$  (Figure 3.3c,g,k,o) and  $\delta$  (Figure 3.3d,h,l,p) phases —  $\gamma$  first and then  $\delta$  — emerge on the surface. They comprise 66 and 100 % carboxylates, respectively.  $\gamma$  and  $\delta$  possess structural and chemical regularities and can form different tilings depending on the ratio of 2H-BDAs, 1H-BDAs, and 0H-BDAs [28]. Roughly speaking, tilings (or tessellations) are periodic patterns of a Euclidian plane consisting of polygons joined by vertices. In our case, the vertices are represented by the centers of BDA molecules; thus, various combinations of the intact, semi-deprotonated, and fully deprotonated molecules can lead to diverse tessellations on the surface (Figure 3.2). For a detailed analysis of BDA self-assembly on Ag(001) at submonolayer coverage, one can address [27, 28].

# 3.2. Phase transformations in a complete monolayer of BDA on Ag(001)

In this section, we present an investigation of BDA self-assembly on Ag(001) at complete-monolayer coverage. When a complete monolayer is deposited, BDA molecules form the  $\alpha$  phase, the same as for submonolayer coverage. After applying thermal annealing, the molecules start to deprotonate, which, in contrast to submonolayer coverage, leads to the

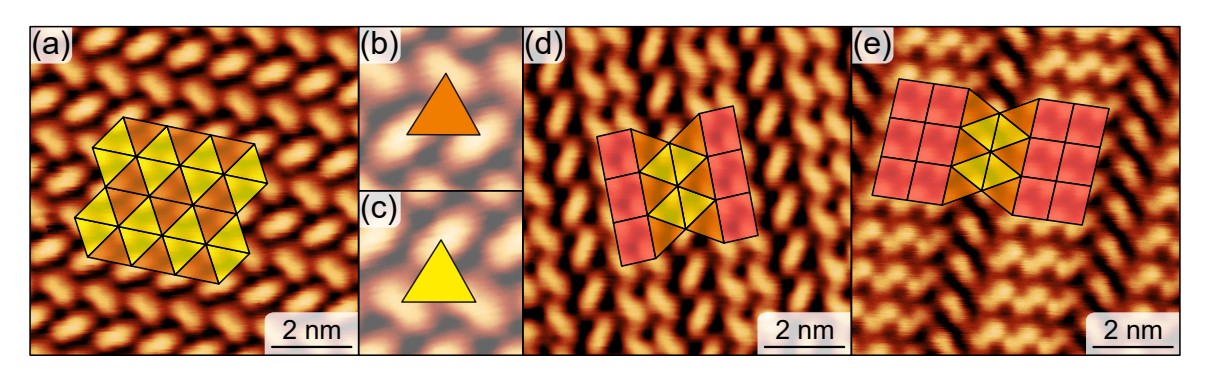


Figure 3.2: BDA tilings on Ag(001). (a) The tiling corresponding to the  $\delta$  phase with appropriate schematic representation overlaid. The representation consists of a combination of triangular tiles. (b, c) The intermolecular binding motif associated with the triangular tiles. (d) The 2-uniform tiling of the γ phase with schematic representation overlaid. In addition to the triangular tiles, γ-tiling also comprises rectangular ones. (e) A 3-uniform tiling constructed by a 1:2:1 mixture of 2H-, 1H-, and 0H-BDAs. This tiling belongs to the phase which we call  $\gamma_3$ .  $\gamma_3$  is similar to γ but has three molecules in the row between the side 0H-BDAs instead of two, where the central molecule of the three is fully protonated. The figure is adapted from [28].

transformation of  $\alpha$  into the so-called  $\dot{\alpha}$  phase. Chemically,  $\dot{\alpha}$  is similar to  $\beta$  containing 50 % of semi-deprotonated and 25 % of fully deprotonated BDAs. However, structurally,  $\dot{\alpha}$  is very close to  $\alpha$ . This is so because the carboxyl-carboxylate binding motif appearing as a result of the deprotonation induces only minor positional changes of BDA in the conditions of spatial constraints. In addition to the main diffraction spots associated with  $\alpha$  (Figure 3.3a), the diffraction of  $\dot{\alpha}$  contains extra spots resembling a moiré (see the following publication). These extra spots indicate the periodicity related to a pattern repeating every 5 BDA molecules per 24 Ag atoms within one molecular chain. We assume that the pattern is induced by the binding of the carboxylates in every 5th BDA molecule to the substrate. As a result,  $\dot{\alpha}$  has an intrachain periodicity. This intrachain periodicity does not ensure that the length of hydrogen bonding between molecules within the chain is the same. It can still vary, which is confirmed by the absence of the diffraction spots associated with the intermolecular distance within a chain and our STM data (see the following publication).

Since  $\dot{\alpha}$  is not an equilibrium structure, it leans to transform to the  $\beta$  phase, but the transformation is only possible when there is some free space on the substrate due to the larger unit cell of  $\beta$ . Indeed, when coverage is slightly less than a complete monolayer (~0.97 ML), the voids are filled with the growing  $\beta$  phase. However, if coverage equals or exceeds a complete monolayer a little bit, we observe the transformation of  $\dot{\alpha}$  into a new phase that resembles  $\gamma_3$  (Figure 3.2e) but has a smaller unit cell. Since the new phase looks like compressed  $\gamma_3$ , we call it compressed  $\gamma_3$  or  $\gamma_3^c$ .  $\gamma_3^c$  begins nucleating at numerous places within the  $\dot{\alpha}$  layer. The preferential nucleation sites include but are not limited to surface defects (e.g., substrate step edges and molecular domain boundaries). The growing  $\gamma_3^c$  clusters cause the fragmentation of the  $\dot{\alpha}$  layer into small  $\gamma_3^c$  domains with the domains' orientation being dependent on the parent phase orientation. The growth itself proceeds in a jump-like fashion and involves a few steps. Each step has distinct inception, domain-growth, and termination stages. It is worth mentioning that the transformation

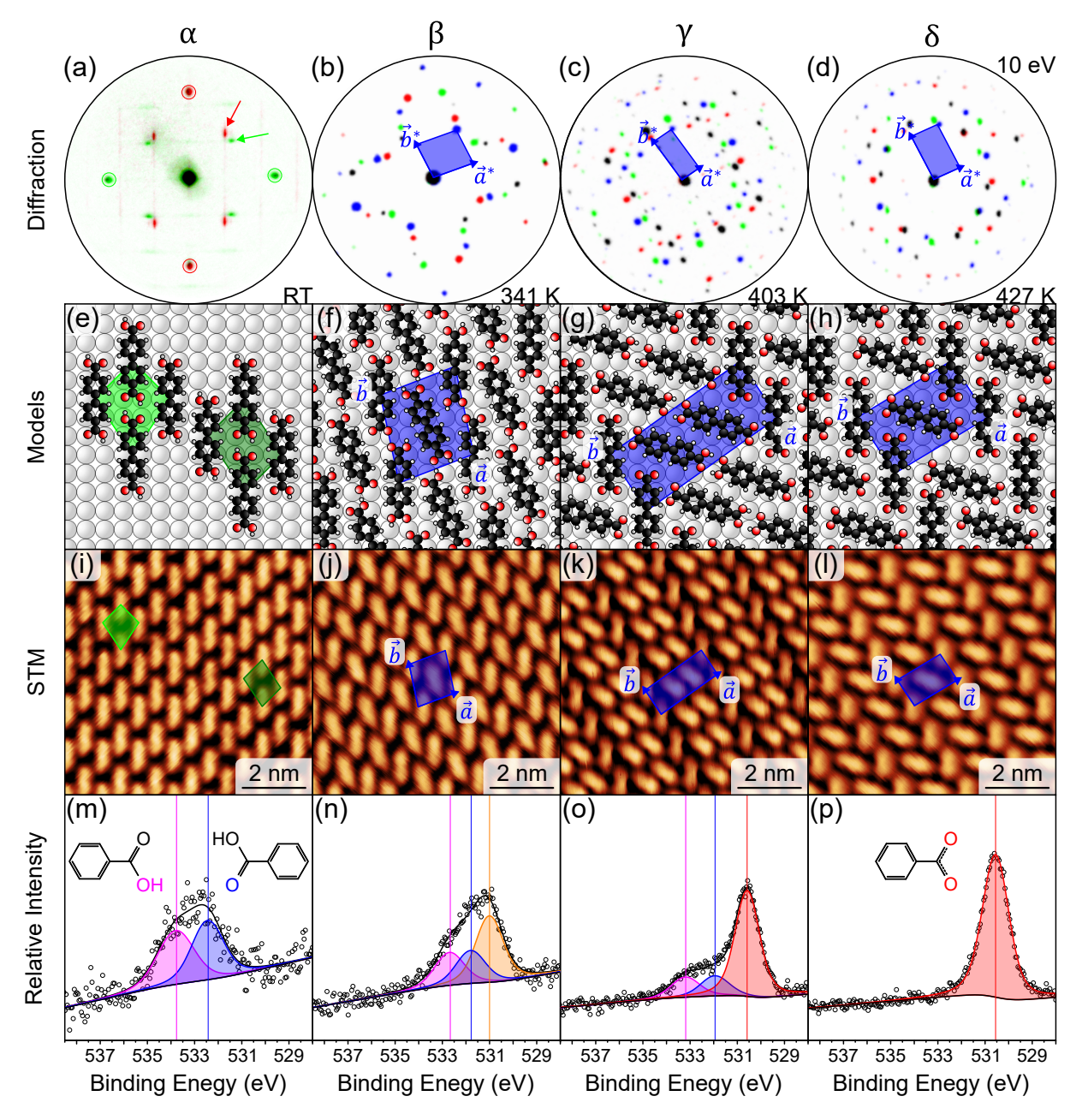


Figure 3.3: BDA self-assembly on Ag(001) at submonolayer coverage. (a–d) The diffraction patterns of the four main phases with the corresponding reciprocal unit cells. Each pattern has been measured at 10 eV. The different colors of the diffraction spots represent the rotational domains of the phases appearing due to the substrate's symmetry. Temperatures at the lower right corners indicate when the transformation into the appropriate phase begins. RT is room temperature. The circles and arrows in (a) mark the diffraction spots associated with the interchain periodicity and BDA dimers of α, respectively. (e–h) The structural models of the main phases with corresponding unit cells. The two possible tiles (not unit cells) of the α phase are shown in (e). (i–l) STM of the main phases with the highlighted unit cells. The α tiles are presented in (i). (m–p) XPS O 1s region measured on BDA main phases at Ag(001). The colors of the peaks align with the different chemical states of O emphasized at the structural formulas in (m) and (p). The orange peak in (n) corresponds to carboxylate oxygen in the β phase.

into the  $\gamma_3^c$  phase also happens for a mixture of  $\dot{\alpha} + \beta$  when coverage is slightly below a submonolayer. In this case,  $\dot{\alpha} \to \gamma_3^c$  transformation occurs first, which leads to inclusions of  $\beta$  in  $\gamma_3^c$ .  $\dot{\alpha} \to \gamma_3^c$  is followed by the transformation of the residual  $\beta$  agglomerates into  $\gamma_3^c$ , i.e.,  $\gamma_3^c$  grows by "engulfing" the adjacent  $\beta$  phase.

When the subsequent deprotonation affects more than 50 % of the BDA carboxyl groups, the forming carboxylates, if placed head-to-head, begin to repeal each other. This leads to the partial desorption of the molecules and, as a result, decreased coverage with some free space on the surface. With the free space available, the following transformation proceeds to the already familiar and thermodynamically favorable  $\gamma$  and  $\delta$  phases depicted in Figure 3.3.

#### The publication:

Procházka, P., Kormoš, L., Shahsavar, A., Stará, V., Makoveev, A.O., Skála, T., Blatnik, M., and Čechal, J. Phase transformations in a complete monolayer of 4,4-biphenyl-dicarboxylic acid on Ag(001). *Applied Surface Science*, 547: 149115, 2021. ISSN: 01694332. Doi: 10.1016/j.apsusc.2021.149115.

### 4. Role of substrate orientation in onsurface molecular self-assembly

Another critical variable in the "equation" of on-surface molecular self-assembly is the substrate. When researchers investigate the influence of the substrate on self-assembly, the primary parameter being considered is usually substrate material, and only a little attention is paid to substrate orientation. However, substrate orientation can have a substantial impact on on-surface processes. Therefore, it would be valuable to extend our knowledge about BDA behavior on different crystal facets. In this regard, we present the following section devoted to a comparative study of BDA self-assembly on Ag(001) and Ag(111) single crystals.

# 4.1. Role of phase stabilization and surface orientation in BDA self-assembly and transformation on silver substrates

Below, we provide a short description of the main ideas presented in the publication of this section. BDA on Ag(111) at submonolayer coverage forms four phases. For the sake of clarity, we denote them  $\alpha^{(111)}$ ,  $\alpha_s^{(111)}$ ,  $\beta^{(111)}$ , and  $\delta^{(111)}$ , where the upper index highlights the substrate's orientation. In the same vein, we assign  $\alpha^{(001)}$ ,  $\dot{\alpha}^{(001)}$ ,  $\beta^{(001)}$ ,  $\gamma^{(001)}$ , and  $\delta^{(001)}$  to the BDA phases on Ag(001).

The as-deposited  $\alpha^{(111)}$  phase comprising only intact fully protonated molecules has a very close structure to  $\alpha^{(001)}$ . It consists of adjacent molecular rows with molecules arranged in a head-to-head fashion. Unlike  $\alpha^{(001)}$ ,  $\alpha^{(111)}$  is periodic with a parallelogram unit cell. However, the diffraction spots affiliated with the periodicity are elongated, which indicates some variation in molecular positioning on the surface. This is caused by the flexible hydrogen bonding between molecules and the weak van-der-Waals molecule-substrate interaction. Morphologically,  $\alpha^{(111)}$  assembles into needle-like BDA islands, whose long side is aligned with the molecular rows constituting them.

The thermal annealing of  $\alpha^{(111)}$  at 373 K during ~100 seconds leads to the emergence of the  $\alpha_s^{(111)}$  phase. Structurally,  $\alpha_s^{(111)}$  is similar to  $\alpha^{(111)}$  but has sharper diffraction spots, moiré pattern, larger molecular islands, and involves deprotonated BDAs. The sharper diffraction spots are the reason for the s subscript in the phase's notation. During the annealing, deprotonated BDA molecules build up within  $\alpha^{(111)}$  islands, first as defects, and later, if the number of deprotonated BDAs overcomes the necessary limit, as the structural units of the newly appearing  $\alpha_s^{(111)}$ . Since deprotonated BDA interacts with the substrate

stronger than non-deprotonated, the molecule-substrate binding begins prevailing the molecule-molecule one for  $\alpha_s^{(111)}$ , and, therefore, the structure of  $\alpha_s^{(111)}$  is more strongly modulated by the substrate than the structure of the initial  $\alpha^{(111)}$ . This makes  $\alpha_s^{(111)}$  more ordered with the sharper diffraction spots and present moiré pattern. The transformation from  $\alpha^{(111)}$  to  $\alpha_s^{(111)}$  proceeds inside of existing  $\alpha^{(111)}$  islands. Besides, the transformation includes Ostwald ripening, that is, large molecular islands grow due to the dissolution of small ones in their vicinity. As a result, the average island size in  $\alpha_s^{(111)}$  is four times larger than in  $\alpha^{(111)}$ . If compared to the phases on Ag(001),  $\alpha_s^{(111)}$  is structurally and chemically analogous to  $\dot{\alpha}^{(001)}$  at complete-monolayer coverage and chemically is similar to  $\beta^{(001)}$  at submonolayer coverage.

Further annealing at  $\sim 400$  K induces the irreversible transition from  $\alpha_s^{(111)}$  to  $\beta^{(111)}$ . The  $\beta^{(111)}$  phase contains  $\sim 63$  % of carboxylate groups and is close to  $\gamma^{(001)}$  by this value having  $\sim 66$  % of the groups. However, the structure of  $\beta^{(111)}$  represents an interlocked molecular configuration with alternating planar and buckled BDAs, which resembles the structure of  $\beta^{(001)}$ . But in contrast to  $\beta^{(001)}$ , the unit cell of  $\beta^{(111)}$  is considerably larger and contains four molecules instead of two. An analysis based on the chemical composition of  $\beta^{(111)}$  indicates that five of eight carboxyl groups in the unit cell are deprotonated. Morphologically,  $\beta^{(111)}$  molecular islands are round-shaped and can extend over several terraces, thus crossing step edges on the surface.

The fully deprotonated  $\delta^{(111)}$  phase is obtained when the sample is annealed at 453 K. Moreover, the complete transformation of  $\beta^{(111)}$  into the on-surface molecular gas is necessary for  $\delta^{(111)}$  to condense (the only exception is when the transformation is carried out at coverage close to a complete monolayer). A microscale analysis reveals the largest single-domain BDA islands we have ever observed at submonolayer coverage. The structures of  $\delta^{(111)}$  and  $\delta^{(001)}$  are almost identical, with the only difference being the size of the unit cells. In general, the interaction of BDA with Ag(111) is believed to be weaker than with Ag(001). The phase transformation times and temperatures confirm that: the  $\alpha^{(001)} \to \dot{\alpha}^{(001)}$  transformation reaches the same degree of deprotonation more quickly and at lower annealing temperatures compared to  $\alpha^{(111)} \to \alpha_s^{(111)}$ .

The remarkable phenomenon we have discovered in this study is what we call burst transformation. It involves La Meer burst nucleation, the stabilization of the deprotonated state within the emerging molecular islands, and rapid deprotonation outside these islands. An example of such transformation is  $\beta^{(111)} \to \delta^{(111)}$  at high coverage close to a complete monolayer. The  $\beta^{(111)}$  phase nucleates when the supersaturation of deprotonated BDA molecules reaches an appropriate level. Once nucleated, clusters of the newly formed phase cause a drop in the supersaturation, and the deprotonation slows down. Interestingly, subsequent thermal annealing leads to an increase in the deprotonation rate but solely outside  $\beta^{(111)}$  clusters. We call this effect the phase stabilization of a deprotonated state. As a result, the supersaturation starts building up due to the increased number of deprotonated BDAs in the on-surface molecular gas. After passing the critical supersaturation level, the  $\delta^{(111)}$  phase forms. During the growth,  $\delta^{(111)}$  first absorbs deprotonated BDAs from the molecular gas, lowering the supersaturation, and then induces the detachment and deprotonation of the molecules constituting  $\beta^{(111)}$  (in other words  $\delta^{(111)}$  dissolves  $\beta^{(111)}$ ). Combining the above-described sequential processes within an irreversible phase transition allows us to develop the term burst transformation.

In general, BDA on Ag(001) and Ag(111) demonstrates similar behavior for the

intact and fully deprotonated phases, whereas the intermediate phases differ significantly. Apart from that, the kinetics of the phase transformations varies quite noticeably on the two substrates. This points out the importance of substrate orientation for the design of self-assembled molecular systems on surfaces. Application-wise, the knowledge of the properties related to substrate orientation can be used in diverse fields, e.g., heterogeneous catalysis, where elementary chemical reactions (including molecular self-assembly) on different facets of catalytic particles are of primary interest.

#### The publication:

Makoveev, A.O., Procházka, P., Blatnik, M., Kormoš, L., Skála, T., and Čechal, J. Role of Phase Stabilization and Surface Orientation in 4,4-Biphenyl-Dicarboxylic Acid Self-Assembly and Transformation on Silver Substrates. *The Journal of Physical Chemistry C*, 126(23): 9989-9997, 2022. ISSN: 1932–7447. DOI: 10.1021/acs.jpcc.2-c02538.

# 5. Non-thermal activation of surface processes

The subject of non-thermal activation of surface processes shows significant interest since it is related to the thermodynamics and kinetics of on-surface molecular self-assembly and synthesis. All temperature-dependent processes have certain activation energies and obey the Boltzmann distribution. Therefore, their rates are strictly determined by the hierarchy of activation energies. Having at disposal only thermal annealing as the activation stimulus does not provide any possibility to adjust the rates in a flexible manner, meaning that all the rates increase if the temperature goes up and decrease if the temperature goes down.

A promising solution to overcome this drawback is non-thermal activation sources. In this chapter, we, first of all, focus on the non-thermal activation tools intended for on-surface chemical reactions. Among such tools, the most widely used are the STM tip, light and e-beam irradiation. As it has already been known for some time, the STM tip represents a precise means for conducting experiments with single molecules (e.g., molecule separation, fusion, molecular diffusion, etc.). The main disadvantage of this approach is its very limited spatial application and the impossibility of its economically effective scaling. In contrast, the light and e-beam irradiation methods can be efficiently applied on large areas and easily scaled. If we compare photons and electrons as the source of the activation stimuli, the former have the diffraction limit of spatial resolution and are relatively expensive to generate (laser irradiation). Electrons, in turn, have much shorter wavelengths and are quite cheap to generate. Despite that, their usage is considered to cause too much damage to on-surface material, especially to sensitive organic compounds. Even low-energy electrons <20 eV are assumed to behave in this way.

In the following publication, we would like to debate this opinion and demonstrate that the fine-tuning of e-beam energy allows non-damaging chemical transformations even of delicate organic molecules. Additionally, we discuss the kinetics of e-beam-induced BDA deprotonation on Ag substrates and describe new molecular phases unattainable by thermal annealing.

## 5.1. Kinetic control of self-assembly using a low-energy electron beam

As presented in Chapter 3 and 4, the thermal annealing of BDA on Ag(001) and Ag(111) causes its deprotonation and, as a result, leads to the formation of four main phases on both substrates. At submonolayer coverage on Ag(001), those phases involve  $\alpha^{(001)}$ ,  $\beta^{(001)}$ ,

 $\gamma^{(001)}$ , and  $\delta^{(001)}$ . If the coverage is a complete monolayer,  $\dot{\alpha}^{(001)}$  forms instead of  $\beta^{(001)}$ . In the case of Ag(111), the self-assembling phases are  $\alpha^{(111)}$ ,  $\alpha_s^{(111)}$ ,  $\gamma^{(111)}$ , and  $\delta^{(111)}$  at any coverage. All the phases differ by the ratios of protonated (2H-BDA), half-deprotonated (1H-BDA), and fully deprotonated (0H-BDA) molecules. In this respect,  $\alpha^{(001)}$  and  $\alpha^{(111)}$  consist of exclusively fully protonated BDAs, whereas  $\delta^{(001)}$  and  $\delta^{(111)}$  have only fully deprotonated molecules. The remaining phases have various ratios of 2H-BDAs, 1H-BDAs, and 2H-BDAs between those extremes. As we mentioned at the beginning of this chapter, the thermal activation of on-surface processes (including chemical reactions) does not provide much flexibility in controlling the rates of those processes. Thus, the thermal annealing of BDA with the purpose of its deprotonation also increases the rates of other concurrent on-surface phenomena. To circumvent this constraint, we have applied a low-energy electron beam to induce the deprotonation reaction.

A low-energy e-beam allows the non-thermal fine adjustment of the deprotonation rate without affecting other processes. So, under  $\sim 10$  eV electron irradiation, we have observed that the  $\alpha^{(001)}$  phase transforms first into  $\beta^{(001)}$  and then into  $\varepsilon^{(001)}$ . The  $\varepsilon^{(001)}$  phase is a new BDA phase that comprises solely deprotonated molecules and is not reachable by thermal annealing. Above  $\sim 10$  eV,  $\alpha^{(001)}$  transforms directly into  $\varepsilon^{(001)}$ . Such energy-dependent phase transformation indicates a change in the deprotonation or growth kinetics with varying electron energy.

To reveal the dependence of deprotonation kinetics on e-beam energy, we have attempted to apply three different approaches. Two of them are based on diffraction measurements, and the last one relies on real-space LEEM observations. The first approach deals with the intensity of the diffraction spots associated with the fully deprotonated  $\varepsilon^{(001)}$  phase. The diffraction spots appear when  $\varepsilon^{(001)}$  starts to grow, and their intensity increases as the phase spreads across the surface. Our measurements demonstrate that the higher the electron energy, the sooner the phase emerges and the faster it grows. However, the formation of  $\varepsilon^{(001)}$  at energies below ~10 eV also involves the formation of  $\beta^{(001)}$  first, which makes the analysis complicated. For that reason, we have investigated the diffraction spots of the electron-induced  $\delta^{(111)}$  phase on Ag(111) that assembles without intermediate phases at all energies. Electron-induced  $\delta^{(111)}$  demonstrates a similar behavior to  $\varepsilon^{(001)}$ , i.e., it emerges sooner and grows faster with increasing electron energy. Since the self-assembly of electron-induced  $\delta^{(111)}$  includes the deprotonation of BDA carboxyl groups, on-surface transport, the nucleation of deprotonated molecules, and the subsequent growth of the phase itself, it is not so suitable for distinguishing the e-beam-induced deprotonation kinetics exclusively. Therefore, we have addressed the problem from another angle.

As we know from Chapter 3, the  $\dot{\alpha}^{(001)}$  phase forms at complete-monolayer coverage, and its formation does not require nucleation and growth, only minor spatial shifts within the existing structure. E-beam irradiation causes the same transformations even at submonolayer coverage. Thus, we have decided to use the intensity of  $\dot{\alpha}^{(001)}$  diffraction spots as the indicators of the deprotonation reaction. When the irradiation begins, the intensity of those diffraction spots increases. This corresponds to a growing number of deprotonated carboxyl groups and, as a result, to a more ordered structure due to the appearing carboxylate-substrate bonds. After a certain time, the intensity reaches a maximum and starts dropping down. We relate this behavior to the instabilities of the  $\dot{\alpha}^{(001)}$  phase manifesting themselves when the critical number of carboxylates is achieved. Such instabilities could be formed, for example, by the deprotonation of a carboxyl group next to

an already existing carboxylate, which would lead to the mutual repulsion of the adjacent BDA molecules containing these groups. We have determined the deprotonation rate as the inverse time from the beginning of the irradiation to the moment when the maximum diffraction-spot intensity appears. Our results demonstrate that the deprotonation rate starts rising at 7 eV and continues increasing with e-beam energy going up. The range between 7 eV and at least 15 eV can be linearly fit, hinting at a non-Arrhenius-like type of kinetics. The offset and subsequent growth of the deprotonation rate with respect to electron energy are consistent with the measurements for the fully deprotonated phases described above.

The third approach we tried was to estimate the intensity of molecular islands in the bright-field LEEM mode. The real-space measurements have the advantage that they can be performed at low energies, down to  $\sim 1$  eV, compared to diffraction experiments, in which the desired diffraction spots are not observed at energies below  $\sim 6$  eV because the Ewald sphere is too small. While BDA islands are being irradiated, we observe a decrease in their real-space intensity, which points out some physical processes taking place in the islands. We have hypothesized that this could be related to the change in BDA's work function due to its deprotonation and the carboxylate-oxygen-surface bond formation. To test the hypothesis, we performed calibration experiments. They involved the e-beam-independent deprotonation of BDA molecules with the subsequent measurement of the intensity at the first moment after opening the LEEM shutter between the sample and the e-beam. It turns out that for some electron energies, the calibration experiments demonstrate an opposite intensity change with respect to the continuous irradiation experiments. This suggests the existence of an alternative/additional mechanism for the intensity, where the intensity depends on some other physical effects in addition to the density of deprotonated BDAs. Further research is needed to reveal the exact mechanism and relate the deprotonation reaction with the real-space intensity.

The deprotonation itself is a complex process comprising a few steps: O-H bond dissociation, escaping the H atom from the reaction site, the on-surface diffusion of H, and its associative desorption. To distinguish the electron-induced O-H dissociation from other concurrent steps and reveal the impact of temperature on it, we have carried out a series of experiments. The experiments included X-ray irradiation of the BDA  $\dot{\alpha}^{(001)}$  structure and XPS measurements. It is known that X-rays generate a substantial number of secondary electrons in a metal substrate; therefore, we expected that those electrons would induce the deprotonation reaction. And indeed, during a continuous long-lasting XPS measurement  $(\sim 30 \text{ h})$  of a complete BDA layer at room temperature (RT), we observed the development of a peak at 531 eV corresponding to the carboxyl-carboxylate bonding within the  $\dot{\alpha}^{(001)}$ phase. The intensity of the peak increased with irradiation. To disclose the thermal contribution to the deprotonation, we have also conducted ten-minute XPS measurements each hour within  $\sim 30$  hours. The final result (after 300 minutes of irradiation in total) shows that only  $\sim 8\%$  of the carboxyl groups are deprotonated, which clearly indicates a negligible thermal contribution at RT on the deprotonation reaction. XPS spectra acquired during continuous experiments but at low temperatures <200 K, demonstrate a two-times decrease in the deprotonation rate compared to RT. However, when the samples were heated up, we first noticed a jump in the deprotonation rate around 210 K to a value higher than at RT and then gradual convergence to the RT value. The resulting fraction of carboxylates was always the same regardless of the temperature history. When we conducted the measurements at the lowest temperatures among all our experiments ( $\lesssim 100$  K), a decrease in the deprotonation rate was even more pronounced. Additionally, we observed an increase in the O 1s signal. This behavior is probably due to the adsorption of water at lower temperatures.

From the sequence of our experiments, we have discovered that the deprotonation rate does not change in the range from 100 to 200 K and approaches the RT value at temperatures >200 K. This means that there is a sudden transition from the low-temperature deprotonation rate to the RT one around 200–210 K. The reason for that is the H associative desorption that requires temperatures above 200 K to be activated. At the low temperatures, the dissociated H atom stays in the vicinity of the parent O atom making the XPS spectra show essentially no difference. But when the temperature rises above 200 K, there is rapid associative desorption of H, which causes a jump in the measured degree of deprotonation and, consequently, in the rate of deprotonation. DFT calculations support our ideas, revealing that the dissociated H atom staying bound to the parent O atom has  $\sim$ 0.6 eV activation energy to leave this position. 0.6 eV corresponds to the associative H desorption above 200 K (assuming that the desorption rate is equal to  $10^{-3}$  s<sup>-1</sup> and the prefactor is  $10^{13}$  s<sup>-1</sup>). The combined experimental and theoretical investigation demonstrates that the secondary electrons generated by XPS can induce the deprotonation reaction while other concurrent processes are still controlled by temperature.

As we remember from Chapter 1, the main e-beam-induced reaction channels involve electron impact ionization (EII), electron impact excitation (EIE), and dissociative electron attachment (DEA). EII and EIE are non-resonant processes manifesting themselves at ≥10 eV and 6 eV, respectively. DEA is a resonant process, which usually happens at lower energies (up to ~15 eV). Since we cannot clearly resolve any resonance peaks in the deprotonation rate dependent on the electron energy curve, we suppose that the main reaction channels inducing the deprotonation reaction are EII and EIE. This work serves as the first step toward discovering electron-activated reactions in single-layer molecular films that can be useful in on-surface molecular self-assembly and synthesis. There are some questions this research has not touched upon and which have to be addressed in future work. To name a few, what is the role of secondary electrons and plasmons in chemical transformations on surfaces? How does the substrate influence such reactions when molecules are strongly bound to the surface? How is real-space LEEM intensity linked to the chemical modifications of on-surface organic layers? Many of them will hopefully be answered someday.

#### The publication:

Makoveev, A.O., Procházka, P., Shahsavar, A., Kormoš, L., Krajňák, T., Stará, V., and Čechal, J. Kinetic control of self-assembly using a low-energy electron beam. *Applied Surface Science*, 600: 154106, 2022. ISSN: 01694332. DOI: 10.1016/j.apsusc.2022.154106.

#### Conclusions

The goal of the thesis was to discuss the influence of diffusion-limited conditions, surface-plane orientation, and the non-thermal activation of the deprotonation reaction on the self-assembly of 4,4'-biphenyldicarboxylic acid on Ag substrates. To achieve this goal, we conducted our experiments in a UHV cluster and applied an integrated analysis involving STM, XPS, LEEM/LEED, and DFT calculations. Below, we summarize the results and highlight the main findings discovered within the research work presented in this thesis.

The self-assembly of BDA in diffusion-limited conditions was studied by employing high molecular coverage on a Ag(001) crystal. We used the high coverage since it prevents the on-surface diffusion of free BDA molecules. The research demonstrates that the deprotonation reaction also happens in diffusion-limited conditions and leads to a new compact BDA phase, which we call  $\dot{\alpha}$ .  $\dot{\alpha}$  is very similar to the as-deposited fully protonated  $\alpha$  structurally but can have various fractions of deprotonated carboxyl groups. Since the interaction of the substrate with deprotonated carboxyl groups is stronger than with nondeprotonated ones, the structure of  $\dot{\alpha}$  is more strongly modulated by Ag(001) and hence has some additional periodicity compared to  $\alpha$ . In particular, we have discovered that  $\dot{\alpha}$ has a pattern that repeats every 5 BDA molecules per 24 Ag atoms in the same molecular chain. The additional periodicity manifests itself in  $\dot{\alpha}$ 's diffraction by extra spots nearby the main  $\alpha$  spots. Since the  $\dot{\alpha}$  phase is not an equilibrium phase, it tends to transform into  $\beta$ , but the transformation is only possible when there is free room on the surface. If the coverage is a complete monolayer,  $\dot{\alpha}$  irreversibly transits to compressed  $\gamma_3^c$ . When the fraction of deprotonated carboxyl groups passes 50 %, BDA starts partially desorbing due to the repulsive interaction between neighboring carboxylates. This causes the emergence of free space on the surface and, as a result, makes the subsequent transformations into more deprotonated phases happen in the same way as they proceed at submonolayer coverage. Insight into molecular self-assembly in diffusion-limited conditions sheds light on the fundamental processes taking place in thin-film fabrication and, therefore, is highly relevant not only for scientific knowledge but also for industrial applications.

To reveal the impact of surface-plane orientation on BDA self-assembly, we conducted a study where the self-assembly was compared on Ag(001) and Ag(111) substrates. Our results demonstrate that BDA forms four molecular phases on Ag(111). For the sake of clarity, we denoted them  $\alpha^{(111)}$ ,  $\alpha_s^{(111)}$ ,  $\beta^{(111)}$ , and  $\delta^{(111)}$ . In the same manner, we termed the BDA phases on Ag(001):  $\alpha^{(001)}$ ,  $\dot{\alpha}^{(001)}$ ,  $\dot{\beta}^{(001)}$ ,  $\gamma^{(001)}$ , and  $\delta^{(001)}$ . The structures of the as-deposited fully protonated ( $\alpha^{(111)}$  and  $\alpha^{(001)}$ ) and fully deprotonated ( $\alpha^{(111)}$  and  $\alpha^{(001)}$ ) phases are very similar, with only minor differences. Those differences are: (i) unlike  $\alpha^{(001)}$ ,  $\alpha^{(111)}$  is periodic, (ii) the unit cell sizes of  $\delta^{(111)}$  and  $\delta^{(001)}$  are different. The intermediate phases ( $\alpha_s^{(111)}$ ,  $\beta^{(111)}$  and  $\dot{\alpha}^{(001)}$ ,  $\beta^{(001)}$ ,  $\gamma^{(001)}$ ), on the contrary, vary substantially.  $\alpha_s^{(111)}$ 

is close to  $\alpha^{(111)}$  structurally, but chemically similar to  $\beta^{(001)}$ . The  $\beta^{(111)}$  phase has  $\sim 63~\%$  of deprotonated carboxyl groups and resembles  $\gamma^{(001)}$  in this regard ( $\sim 66~\%$  of the groups). In terms of the structure,  $\beta^{(111)}$  has an interlocked molecular configuration similar to  $\beta^{(001)}$ , but with a much larger unit cell. During the research, we also discovered an interesting effect, which we called burst transforamation. The burst transforamation relates to an irreversible phase transition and involves La Meer burst nucleation of a new phase, the stabilization of a molecular chemical state inside new-phase clusters (for BDA, this is a deprotonation state), and fast chemical conversion outside these clusters (for BDA, this is the deprotonation reaction). The results clearly emphasize the significance of surface-plane orientation in molecular self-assembly on surfaces and bear a high potential to be used in the fields where the understanding of elementary chemical steps on different particle facets is important (e.g., heterogeneous catalysis).

As discussed in the thesis, the activation of on-surface processes by thermal annealing does not allow tweaking the rate hierarchy of those processes. In this respect, non-thermal activation sources are the potential means to bypass this drawback. Hence, we conducted a study where the BDA deprotonation reaction on Ag substrates was induced by a low-energy electron beam. The results demonstrate that BDA takes different self-assembly pathways at different electron energies. In particular, the  $\alpha^{(001)}$  phase transforms first into  $\beta^{(001)}$ and then into  $\varepsilon^{(001)}$  below  $\sim 10$  eV and directly into  $\varepsilon^{(001)}$  above  $\sim 10$  eV e-beam irradiation.  $\varepsilon^{(001)}$  is a new phase we have discovered in this work that is inaccessible by thermal annealing. We also estimated the electron-energy-dependent kinetics of the deprotonation via the intensity of the diffraction spots associated with  $\dot{\alpha}^{(001)}$ .  $\dot{\alpha}^{(001)}$  has been chosen since its formation does not require considerable spatial movements of molecules and, therefore, is predominantly influenced by the deprotonation reaction and not by other parallel processes, such as diffusion, nucleation, BDA attachment, and detachment, etc. It turns out that the deprotonation rate increases with the energy going up and can be linearly fit at least in the range of 7–15 eV. The deprotonation is an integrated phenomenon, which involves O-H bond dissociation, escaping the H atom from the reaction site, the on-surface diffusion of H, and its associative desorption. To distinguish the O-H dissociation from the other processes and disclose its dependence on temperature, we conducted a series of temperature-variable XPS measurements. Our findings suggest that the dissociation process is temperature independent and can be induced by electrons (as it was induced by secondary electrons in the XPS measurements). Additionally, we assume the H associative desorption, which starts at  $\sim 200$  K, to be the rate-limiting step of the deprotonation reaction at lower temperatures. Although a great deal of work has been accomplished, there are still some loose ends. For example, it would be interesting to find out the role of the substrate in on-surface chemical transformations activated by electrons. How exactly do secondary electrons and plasmons impact those transformations? A methodology allowing one to relate the dynamics of on-surface processes with LEEM intensity changes is also highly desired. We hope that these questions and tasks will be addressed in future research.

#### References

- [1] DE FEYTER, S., GESQUIÈRE, A., ABDEL-MOTTALEB, M. M., GRIM, P. C. M., DE SCHRYVER, F. C., MEINERS, C., SIEFFERT, M., VALIYAVEETTIL, S., and MÜLLEN, K. Scanning Tunneling Microscopy: A Unique Tool in the Study of Chirality, Dynamics, and Reactivity in Physisorbed Organic Monolayers. *Accounts of Chemical Research*, 33(8): 520–531, 2000. ISSN: 0001-4842. DOI: 10.1021/ar970040g.
- [2] DE FEYTER, S. and DE SCHRYVER, F. C. Two-dimensional supramolecular self-assembly probed by scanning tunneling microscopy. *Chemical Society Reviews*, 32(3): 139–150, 2003. ISSN: 03060012. DOI: 10.1039/b206566p.
- [3] KUDERNAC, T., LEI, S., ELEMANS, J. A. A. W., and DE FEYTER, S. Two-dimensional supramolecular self-assembly: nanoporous networks on surfaces. *Chem. Soc. Rev.*, 38(2): 402–421, 2009. ISSN: 0306-0012. DOI: 10.1039/B708902N.
- [4] Surin, M., Samorì, P., Jouaiti, A., Kyritsakas, N., and Hosseini, M. W. Molecular Tectonics on Surfaces: Bottom-Up Fabrication of 1D Coordination Networks That Form 1D and 2D Arrays on Graphite. *Angewandte Chemie International Edition*, 46(1-2): 245–249, 2007. ISSN: 14337851. DOI: 10.1002/anie.200603558.
- [5] LINGENFELDER, M. A., SPILLMANN, H., DMITRIEV, A., STEPANOW, S., LIN, N., BARTH, J. V., and KERN, K. Towards Surface-Supported Supramolecular Architectures: Tailored Coordination Assembly of 1,4-Benzenedicarboxylate and Fe on Cu(100). *Chemistry A European Journal*, 10(8): 1913–1919, 2004. ISSN: 0947-6539. DOI: 10.1002/chem.200305589.
- [6] Walch, H., Gutzler, R., Sirtl, T., Eder, G., and Lackinger, M. Material- and Orientation-Dependent Reactivity for Heterogeneously Catalyzed Carbon—Bromine Bond Homolysis. *The Journal of Physical Chemistry C*, 114(29): 12604–12609, 2010. ISSN: 1932-7447. DOI: 10.1021/jp102704q.
- [7] BOUJU, X., MATTIOLI, C., FRANC, G., PUJOL, A., and GOURDON, A. Bicomponent Supramolecular Architectures at the Vacuum–Solid Interface. *Chemical Reviews*, 117(3): 1407–1444, 2017. ISSN: 0009-2665. DOI: 10.1021/acs.chemrev.6b00389.
- [8] Macleod, J. Design and construction of on-surface molecular nanoarchitectures: lessons and trends from trimesic acid and other small carboxlyated building blocks. Journal of Physics D: Applied Physics, 53(4): 043002, 2020. ISSN: 0022-3727. DOI: 10.1088/1361-6463/ab4c4d.
- [9] Shen, Q., Gao, H.-Y., and Fuchs, H. Frontiers of on-surface synthesis: From principles to applications. *Nano Today*, 13: 77–96, 2017. ISSN: 17480132. DOI: 10.1016/j.nantod.2017.02.007.

- [10] Wang, T. and Zhu, J. Confined on-surface organic synthesis: Strategies and mechanisms. *Surface Science Reports*, 74(2): 97–140, 2019. ISSN: 01675729. DOI: 10.1016/j.surfrep.2019.05.001.
- [11] CLAIR, S. and OTEYZA, D. G. de. Controlling a Chemical Coupling Reaction on a Surface: Tools and Strategies for On-Surface Synthesis. *Chemical Reviews*, 119(7): 4717–4776, 2019. ISSN: 0009-2665. DOI: 10.1021/acs.chemrev.8b00601.
- [12] GUTZLER, R., CARDENAS, L., and ROSEI, F. Kinetics and thermodynamics in surface-confined molecular self-assembly. *Chemical Science*, 2(12): 2290, 2011. ISSN: 2041-6520. DOI: 10.1039/c1sc00531f.
- [13] PILENI, M.-P. Self-Assembly of Inorganic Nanocrystals: Fabrication and Collective Intrinsic Properties. *Accounts of Chemical Research*, 40(8): 685–693, 2007. ISSN: 0001-4842. DOI: 10.1021/ar6000582.
- [14] PHILP, D. and STODDART, J. F. Self-Assembly in Natural and Unnatural Systems. Angewandte Chemie International Edition in English, 35(11): 1154–1196, 1996. ISSN: 0570-0833. DOI: 10.1002/anie.199611541.
- [15] Grantcharova, V., Alm, E. J., Baker, D., and Horwich, A. L. Mechanisms of protein folding. *Current Opinion in Structural Biology*, 11(1): 70–82, 2001. ISSN: 0959440X. Doi: 10.1016/S0959-440X(00)00176-7.
- [16] McManus, J. J., Charbonneau, P., Zaccarelli, E., and Asherie, N. The physics of protein self-assembly. *Current Opinion in Colloid & Interface Science*, 22: 73–79, 2016. ISSN: 13590294. DOI: 10.1016/j.cocis.2016.02.011.
- [17] SHAPIRO, J. A. THINKING ABOUT BACTERIAL POPULATIONS AS MULTI-CELLULAR ORGANISMS. *Annual Review of Microbiology*, 52(1): 81–104, 1998. ISSN: 0066-4227. DOI: 10.1146/annurev.micro.52.1.81.
- [18] Bonabeau, E., Dorigo, M., and Theraulaz, G. Inspiration for optimization from social insect behaviour. *Nature*, 406(6791): 39–42, 2000. ISSN: 0028-0836. DOI: 10.1038/35017500.
- [19] Shimoyama, N., Sugawara, K., Mizuguchi, T., Hayakawa, Y., and Sano, M. Collective Motion in a System of Motile Elements. *Physical Review Letters*, 76(20): 3870–3873, 1996. ISSN: 0031-9007. DOI: 10.1103/PhysRevLett.76.3870.
- [20] PAPADOPOULOU, A., LAUCKS, J., and TIBBITS, S. From Self-Assembly to Evolutionary Structures. *Architectural Design*, 87(4): 28–37, 2017. ISSN: 00038504. DOI: 10.1002/ad.2192.
- [21] Wijesinghe, D. B., Hopkins, A. M., Brough, S., Taylor, E. N., Norberg, P., Bauer, A., Brown, M. J. I., Cameron, E., Conselice, C. J., Croom, S., Driver, S., Grootes, M. W., Jones, D. H., Kelvin, L., Loveday, J., Pimbblet, K. A., Popescu, C. C., Prescott, M., Sharp, R., Baldry, I., Sadler, E. M., Liske, J., Robotham, A. S. G., Bamford, S., Bland-Hawthorn, J., Gunawardhana, M., Meyer, M., Parkinson, H., Drinkwater, M. J., Peacock, J., and Tuffs, R. Galaxy And Mass Assembly (GAMA): galaxy environments and star formation rate variations. *Monthly Notices of the Royal Astronomical Society*, 423(4): 3679–3691, 2012. ISSN: 00358711. Doi: 10.1111/j.1365-2966.2012.21164.x.

- [22] WHITELAM, S. and JACK, R. L. The Statistical Mechanics of Dynamic Pathways to Self-Assembly. *Annual Review of Physical Chemistry*, 66(1): 143–163, 2015. ISSN: 0066-426X. DOI: 10.1146/annurev-physchem-040214-121215.
- [23] KÜHNLE, A. Self-assembly of organic molecules at metal surfaces. Current Opinion in Colloid & Interface Science, 14(2): 157–168, 2009. ISSN: 13590294. DOI: 10.1016/j.cocis.2008.01.001.
- [24] BARTH, J. V., COSTANTINI, G., and KERN, K. Engineering atomic and molecular nanostructures at surfaces. *Nature*, 437(7059): 671–679, 2005. ISSN: 0028-0836. DOI: 10.1038/nature04166.
- [25] CLAIR, S., PONS, S., SEITSONEN, A. P., BRUNE, H., KERN, K., and BARTH, J. V. STM Study of Terephthalic Acid Self-Assembly on Au(111): Hydrogen-Bonded Sheets on an Inhomogeneous Substrate. *The Journal of Physical Chemistry B*, 108(38): 14585–14590, 2004. ISSN: 1520-6106. DOI: 10.1021/jp049501n.
- [26] PEARCE, N. and CHAMPNESS, N. R. "Surface Self-Assembly of Hydrogen-Bonded Frameworks". In: *Supramolecular Chemistry on Surfaces*. Wiley, Mar. 2022, 199–218. DOI: 10.1002/9783527816699.ch9.
- [27] PROCHÁZKA, P., GOSALVEZ, M. A., KORMOŠ, L., TORRE, B. de la, GALLARDO, A., ALBERDI-RODRIGUEZ, J., CHUTORA, T., MAKOVEEV, A. O., SHAHSAVAR, A., ARNAU, A., JELÍNEK, P., and ČECHAL, J. Multiscale Analysis of Phase Transformations in Self-Assembled Layers of 4,4 -Biphenyl Dicarboxylic Acid on the Ag(001) Surface. ACS Nano, 14(6): 7269–7279, 2020. ISSN: 1936-0851. DOI: 10.1021/acsnano.0c02491.
- [28] KORMOŠ, L., PROCHÁZKA, P., MAKOVEEV, A. O., and ČECHAL, J. Complex kuniform tilings by a simple bitopic precursor self-assembled on Ag(001) surface. *Nature Communications*, 11(1): 1856, 2020. ISSN: 2041-1723. DOI: 10.1038/s41467-020-15727-6.
- [29] POOLE, P. H., SCIORTINO, F., ESSMANN, U., and STANLEY, H. E. Phase behaviour of metastable water. *Nature*, 360(6402): 324–328, 1992. ISSN: 0028-0836. DOI: 10.1038/360324a0.
- [30] LOHMANN, U., SPICHTINGER, P., JESS, S., PETER, T., and SMIT, H. Cirrus cloud formation and ice supersaturated regions in a global climate model. *Environmental Research Letters*, 3(4): 045022, 2008. ISSN: 1748-9326. DOI: 10.1088/1748-9326/3/4/045022.
- [31] Khan, S. R., Glenton, P. A., Backov, R., and Talham, D. R. Presence of lipids in urine, crystals and stones: Implications for the formation of kidney stones. *Kidney International*, 62(6): 2062–2072, 2002. ISSN: 00852538. DOI: 10.1046/j.1523–1755.2002.00676.x.
- [32] MENDEZ-VILLUENDAS, E. and BOWLES, R. K. Surface Nucleation in the Freezing of Gold Nanoparticles. *Physical Review Letters*, 98(18): 185503, 2007. ISSN: 0031-9007. DOI: 10.1103/PhysRevLett.98.185503.
- [33] WULFF, G. XXV. Zur Frage der Geschwindigkeit des Wachsthums und der Auflösung der Krystallflächen. Zeitschrift für Kristallographie Crystalline Materials, 34(1-6): 449–530, 1901. ISSN: 2196-7105. DOI: 10.1524/zkri.1901.34.1.449.

- [34] Ryu, S. The validity of classical nucleation theory and its application to dislocation nucleation. 2011.
- [35] TROMP, R. M. and HANNON, J. B. THERMODYNAMICS OF NUCLEATION AND GROWTH. Surface Review and Letters, 09(03n04): 1565–1593, 2002. ISSN: 0218-625X. DOI: 10.1142/S0218625X02003846.
- [36] VOLMER, M. and WEBER, A. Keimbildung in übersättigten Gebilden. Zeitschrift für Physikalische Chemie, 119U(1): 277–301, 1926. ISSN: 2196-7156. DOI: 10.1515/zpch-1926-11927.
- [37] FARKAS, L. Keimbildungsgeschwindigkeit in übersättigten Dämpfen. Zeitschrift für Physikalische Chemie, 125U(1): 236–242, 1927. ISSN: 2196-7156. DOI: 10.1515/zpch-1927-12513.
- [38] BECKER, R. and DÖRING, W. Kinetische Behandlung der Keimbildung in übersättigten Dämpfen. Annalen der Physik, 416(8): 719–752, 1935. ISSN: 00033804. DOI: 10.1002/andp.19354160806.
- [39] ZELDOVICH, Y. B. On the Theory of New Phase Formation: Cavitation. *Acta Physicochem.*, USSR, 18: 1, 1943.
- [40] Frenkel, J. Kinetic Theory of Liquids. Oxford at the Clarendon Press, 1946.
- [41] ZINSMEISTER, G. A contribution to Frenkel's theory of condensation. *Vacuum*, 16(10): 529–535, 1966. ISSN: 0042207X. DOI: 10.1016/0042-207X(66)90349-6.
- [42] ZINSMEISTER, G. Theory of thin film condensation. Part b: Solution of the simplified condensation equation. *Thin Solid Films*, 2(5-6): 497–507, 1968. ISSN: 00406090. DOI: 10.1016/0040-6090(68)90063-1.
- [43] ZINSMEISTER, G. Theory of thin film condensation part C: Aggregate size distribution in island films. *Thin Solid Films*, 4(5): 363–386, 1969. ISSN: 00406090. DOI: 10.1016/0040-6090(69)90100-X.
- [44] ZINSMEISTER, G. Theory of thin film condensation Part D: Influence of a variable collision factor. *Thin Solid Films*, 7(1): 51–75, 1971. ISSN: 00406090. DOI: 10.1016/0040-6090(71)90013-7.
- [45] EVANS, J., THIEL, P., and BARTELT, M. Morphological evolution during epitaxial thin film growth: Formation of 2D islands and 3D mounds. *Surface Science Reports*, 61(1-2): 1–128, 2006. ISSN: 01675729. DOI: 10.1016/j.surfrep.2005.08.004.
- [46] Frankl, D. and Venables, J. Nucleation on substrates from the vapour phase. *Advances in Physics*, 19(80): 409–456, 1970. ISSN: 0001-8732. DOI: 10.1080/00018737000101151.
- [47] VENABLES, J. A. Rate equation approaches to thin film nucleation kinetics. *Philosophical Magazine*, 27(3): 697–738, 1973. ISSN: 0031-8086. DOI: 10.1080/14786437308219242.
- [48] VENABLES, J. A., SPILLER, G. D. T., and HANBUCKEN, M. Nucleation and growth of thin films. *Reports on Progress in Physics*, 47(4): 399–459, 1984. ISSN: 0034-4885. DOI: 10.1088/0034-4885/47/4/002.
- [49] Walton, D. Nucleation of Vapor Deposits. *The Journal of Chemical Physics*, 37(10): 2182–2188, 1962. ISSN: 0021-9606. DOI: 10.1063/1.1732985.

- [50] VICSEK, T. and FAMILY, F. Dynamic Scaling for Aggregation of Clusters. *Physical Review Letters*, 52(19): 1669–1672, 1984. ISSN: 0031-9007. DOI: 10.1103/PhysRevLett. 52.1669.
- [51] AMAR, J. G. and FAMILY, F. Critical Cluster Size: Island Morphology and Size Distribution in Submonolayer Epitaxial Growth. *Physical Review Letters*, 74(11): 2066–2069, 1995. ISSN: 0031-9007. DOI: 10.1103/PhysRevLett.74.2066.
- [52] Winkler, A. On the nucleation and initial film growth of rod-like organic molecules. Surface Science, 652: 367–377, 2016. ISSN: 00396028. DOI: 10.1016/j.susc.2016.02.015.
- [53] ARUMAINAYAGAM, C. R., LEE, H.-L., NELSON, R. B., HAINES, D. R., and GUNAWAR-DANE, R. P. Low-energy electron-induced reactions in condensed matter. *Surface Science Reports*, 65(1): 1–44, 2010. ISSN: 01675729. DOI: 10.1016/j.surfrep.2009.09.001.
- [54] Bald, I., Langer, J., Tegeder, P., and Ingólfsson, O. From isolated molecules through clusters and condensates to the building blocks of life. *International Journal of Mass Spectrometry*, 277(1-3): 4–25, 2008. ISSN: 13873806. DOI: 10.1016/j.ijms. 2008.06.013.
- [55] Torbrügge, S., Schaff, O., and Rychen, J. Application of the KolibriSensor ® to combined atomic-resolution scanning tunneling microscopy and noncontact atomic-force microscopy imaging. Journal of Vacuum Science & Technology B, Nanotechnology and Microelectronics: Materials, Processing, Measurement, and Phenomena, 28(3): C4E12–C4E20, 2010. ISSN: 2166-2746. DOI: 10.1116/1.3430544.
- [56] RAHE, P., BECHSTEIN, R., and KÜHNLE, A. Vertical and lateral drift corrections of scanning probe microscopy images. *Journal of Vacuum Science & Technology B, Nanotechnology and Microelectronics: Materials, Processing, Measurement, and Phenomena*, 28(3): C4E31–C4E38, 2010. ISSN: 2166-2746. DOI: 10.1116/1.3360909.
- [57] KORMOŠ, L., PROCHÁZKA, P., ŠIKOLA, T., and ČECHAL, J. Molecular Passivation of Substrate Step Edges as Origin of Unusual Growth Behavior of 4,4-Biphenyl Dicarboxylic Acid on Cu(001). *The Journal of Physical Chemistry C*, 122(5): 2815–2820, 2018. ISSN: 1932-7447. DOI: 10.1021/acs.jpcc.7b11436.
- [58] Zhu, N., Osada, T., and Komeda, T. Supramolecular assembly of biphenyl dicarboxylic acid on Au(1 1 1). Surface Science, 601(8): 1789–1794, 2007. ISSN: 00396028. DOI: 10.1016/j.susc.2007.02.003.
- [59] Mohr, S., Schmitt, T., Döpper, T., Xiang, F., Schwarz, M., Görling, A., Schneider, M. A., and Libuda, J. Coverage-Dependent Anchoring of 4,4-Biphenyl Dicarboxylic Acid to CoO(111) Thin Films. *Langmuir*, 33(17): 4178–4188, 2017. ISSN: 0743-7463. Doi: 10.1021/acs.langmuir.7b00465.